



日本原子力研究開発機構機関リポジトリ  
Japan Atomic Energy Agency Institutional Repository

Title	Composite behavior of lath martensite steels induced by plastic strain, a new paradigm for the elastic-plastic response of martensitic steels
Author(s)	Ungár T., Harjo S., Kawasaki Takuro, Tomota Yo, Rib¥'arik G., Shi Z.
Citation	Metallurgical and Materials Transactions A, 48(1), p.159-167
Text Version	Author's Post-print
URL	<a href="https://jopss.jaea.go.jp/search/servlet/search?5057566">https://jopss.jaea.go.jp/search/servlet/search?5057566</a>
DOI	<a href="https://doi.org/10.1007/s11661-016-3845-4">https://doi.org/10.1007/s11661-016-3845-4</a>
Right	This is a post-peer-review, pre-copyedit version of an article published in Metallurgical and Materials Transactions A]. The final authenticated version is available online at: <a href="http://dx.doi.org/10.1007/s11661-016-3845-4">http://dx.doi.org/10.1007/s11661-016-3845-4</a> .



1 **Composite behavior of lath-martensite steels induced by plastic strain, a new paradigm for**  
2 **the elastic-plastic response of martensitic steels**

3  
4 Tamás Ungár<sup>1,3\*&</sup>, Stefanus Harjo<sup>2\*</sup>, Takuro Kawasaki<sup>2</sup>, Yo Tomota<sup>4\*\*</sup>, Gábor Ribárik<sup>1,3</sup> and  
5 Zengmin Shi<sup>5</sup>

6  
7 <sup>1</sup>Department of Materials Physics, Eötvös University, Budapest, PO Box 32, H-1518, Hungary

8 <sup>2</sup>J-PARC Center, Japan Atomic Energy Agency, Tokai-mura, Naka-gun, Ibaraki 319-1195, Japan

9 <sup>3</sup>Laboratory of Excellence "DAMAS", Université de Lorraine, Nancy-Metz, F-57045 Metz,  
10 France

11 <sup>4</sup>Graduate School of Science and Engineering, Ibaraki University, 4-12-1 Nakanarusawa,  
12 Hitachi, Ibaraki, 316-8511, Japan

13 <sup>5</sup>College of Materials and Chemical Engineering, China Three Gorges University, Yichang  
14 443002, PR China

15  
16 \*These authors contributed equally

17 \*\* now at National Institute for Materials Science, 1-2-1 Sengen, Tsukuba, Ibaraki, 305-0047,  
18 Japan

19  
20 **ABSTRACT**

21  
22 Based on high-resolution neutron diffraction experiments we will show that in lath-martensite  
23 steels the initially homogeneous dislocation structure, i.e. homogeneous on the length scale of  
24 grain size, is disrupted by plastic deformation, which, in turn, produces a composite on the length  
25 scale of martensite lath-packets. The diffraction patterns of plastically strained martensitic steel  
26 reveal characteristically asymmetric peak profiles in the same way as has been observed in  
27 materials with heterogeneous dislocation structures. The quasi homogeneous lath structure,  
28 formed by quenching, is disrupted by plastic deformation producing a composite structure. Lath  
29 packets oriented favorably or unfavorably for dislocation glide become soft or hard. Two lath  
30 packet types develop by work softening or work hardening in which the dislocation densities  
31 become smaller or larger compared to the initial average dislocation density. The decomposition

32 into soft and hard lath packets is accompanied by load redistribution and the formation of long-  
33 range internal stresses between the two lath packet types. The composite behavior of plastically  
34 deformed lath martensite opens a new way to understand the elastic-plastic response in this class  
35 of materials.

36

37 Keywords: *composite behavior of lath martensite, elastic-plastic response of lath martensite,*  
38 *neutron diffraction line profile analysis, characteristically asymmetric peak profiles, role of*  
39 *mean free path of dislocations*

40 &Corresponding author: [ungar@ludens.elte.hu](mailto:ungar@ludens.elte.hu)

41

42

### 43 **1. Introduction**

44

45 Lath martensitic steels are widely used iron base alloys with outstanding mechanical properties.  
46 They contain carbon varying between a few hundredths to a few tenths of weight percentage and  
47 a variety of different alloying elements in small quantities. Their strength is induced by the  
48 transformation of the fcc  $\gamma$  to the bcc  $\alpha$  phase by fast cooling [1]. Coherency strains in the  
49 quenched alloy induce huge dislocation densities which are the source of the alloy's strength [1].  
50 Though this alloy has been used since the existence of steel, the way its microstructure functions  
51 is still unclarified.

52

53 A typical lath-martensite consists of blocks of lamellar plates, where the blocks form packets [2-  
54 4]. The blocks are subdivided into sub-blocks, where the smallest constituents are lamellar plates  
55 called martensite-laths. The hierarchy of packets, blocks, sub-blocks and laths is shown  
56 schematically in Fig. 1. Within the packets the laths are parallel lamellae each having crystal  
57 orientations separated by different twin-related boundaries. The 110 oriented lath planes align  
58 coherently with one of the 111 type planes of the primary austenite. Within the primary austenite  
59 grain boundary, several packets of different crystallographic orientations can coexist [2-4], see  
60 Fig. 1a.

61

62 Despite the rather large yield stress of martensitic steels, they do show some ductility [1,5-7].  
63 Recent microscale deformation experiments [8,9] have attempted to reveal the microscopic  
64 mechanisms controlling plastic deformation in lath-martensite. Micropillars with a single  
65 martensite block have shown perfectly ideal stress-strain behavior with no strain hardening and a  
66 flow stress of  $\sim 1.2$  GPa. Micropillars with two or more blocks, however, have shown significant  
67 strain hardening with a similarly large yield stress [8]. Microscale tensile experiments have  
68 shown relatively small flow-stress values of the order of  $\sim 350$  MPa, when the active slip systems  
69 were in-lath-plane, whereas the flow-stress almost doubled when the active slip systems were  
70 out-of-lath-plane [9]. The two experiments in [8] and [9] indicated that there might be a load  
71 redistribution between packets in which the active slip systems are in- or out-of-lath-plane,  
72 respectively. This is shown schematically in Fig. 1b, where we can see two packets oriented with  
73 active Burgers vectors either in- or out-of-lath-plane.

74  
75 The present work is based on characteristically asymmetric neutron diffraction profiles. We will  
76 show for the first time that although the microstructures of lath packets in lath-martensitic steels  
77 are similar in the as-quenched initial state, this homogeneity is disrupted during plastic  
78 deformation. The disruption is the result of the process where lath-packets with active Burgers  
79 vectors in-lath-plane work-soften, whereas those with active Burgers vectors out-of-lath-plane  
80 work-harden. Plastic deformation produces coexisting soft and hard lath packets, and the  
81 deformed lath martensite behaves like a composite. The composite behavior could be regarded as  
82 a new paradigm allowing us to understand the elastic-plastic response of lath martensite

83  
84

## 85 2. Experimental

86

87 An as-quenched rod-shape lath martensite steel specimen was tensile deformed in a screw-type  
88 loading machine at a strain rate of  $10^{-5}$  s<sup>-1</sup>. Strain was measured by a strain gauge glued on the  
89 specimen. The composition of the specimen was Fe-0.22C-0.87Si-1.64Mn-0.024Ti-0.0015B-  
90 0.0025N (all in wt.%). The as quenched martensitic steel specimen contained a small amount of  
91 retained austenite of the order of about 3%. Scanning electron microscopy (SEM) images

92 revealed no significant texture. According to the SEM micrographs the average packet and block  
93 sizes were about 20 and 4  $\mu\text{m}$ , respectively. Further details of the specimen will be given in [10].

94  
95 The experiments took place at the TAKUMI beamline of the Materials and Life Science  
96 Experimental Facility of the Japan Proton Accelerator Research Complex, J-PARC. The tensile  
97 machine was placed into the TAKUMI beamline and the neutron diffraction patterns were  
98 collected in-situ during the tensile deformation. The beamline was operated in the high resolution  
99 and high intensity time-of-flight (TOF) mode. High resolution was achieved by tuning the  
100 incident optical devices, especially the neutron guides and collimators, for this purpose. Despite  
101 the loss of intensity, due to high resolution, high intensity was retained since the instrument was  
102 built at a pulsed, high intensity spallation-neutron-source. The schematic outline of the TOF  
103 diffractometer and the specimen geometry are shown in Fig. 2 and will be discussed in more  
104 detail in [10]. The illuminated volume in the specimen was restricted to  $5 \times 5 \times 5 \text{ mm}^3$  by the  
105 incident beam slit and the radial collimators. The instrumental peak width was tuned to 0.3 %.

106  
107 The loading direction and the diffraction vectors were either parallel or perpendicular to each  
108 other regarding the  $+90^\circ$  or the  $-90^\circ$  detectors, i.e. in the 'axial' or the 'side' cases, respectively, as  
109 indicated in Fig. 2. The intrinsic peak asymmetry due to TOF geometry in the TAKUMI  
110 diffractometer produces slightly longer profile tails in the larger  $d$  value directions. This effect,  
111 however, will be neglected, since it is significantly smaller than the asymmetry caused by the  
112 long range internal stresses in the specimen. Details follow in the next paragraph.

113  
114 Strains or stresses, which are related to directions normal to the tensile direction, are often called  
115 radial strains or stresses. In the present work we will call these side-case strains or stresses, since  
116 the same terms were used in earlier literature on long range internal stresses, see Refs. [11-13].

117  
118  
119 **3. Evaluation of asymmetric peak profiles in terms of local dislocation densities and long-**  
120 **range-internal-stresses**

121

122 In order to improve the counting statistics, the deformation was interrupted at 9 consecutive  
123 strain values as shown in the stress-strain curve (see Fig. 3). Line profile analysis has been done  
124 on the diffraction patterns measured in the unloaded states of the specimen. These diffraction  
125 patterns were evaluated by the Convolutional-Multiple-Whole-Profile (CMWP) fitting procedure  
126 based on physically modelled profile functions for dislocations, crystallite size and planar defects  
127 [14,15]. The size profile function,  $I^S$ , is constructed by assuming a logarithmic-normal size  
128 distribution of the coherently scattering domains. The size distribution function is described by  
129 the median,  $m$ , and its variance,  $\zeta$ . The strain profile,  $I^D$ , is based on dislocations characterized by  
130 the average density,  $\rho$ , and the arrangement parameter,  $M$ , where  $M=R_e\sqrt{\rho}$  and  $R_e$  is the  
131 effective outer cut-of radius of dislocations. When the dislocation arrangement has a strong  
132 dipole character, i.e. when their strain field is strongly screened,  $R_e$  will be smaller than the  
133 average dislocation distance and  $M$  becomes smaller than 1 ( $M \leq 1$ ). When, however, the  
134 dislocation arrangement has a weak dipole character, i.e. when the strain field is weakly  
135 screened,  $R_e$  will be larger than the average dislocation distance and  $M$  becomes larger than 1  
136 ( $M \gg 1$ ). Strain broadening is also anisotropic as a function of reflection order, or the  $hkl$  indexes.  
137 This effect is caused by elastic anisotropy of the material. Strain anisotropy is taken into account  
138 by the contrast factors,  $C$ , of the different  $hkl$  diffraction profiles. When the texture is not strong  
139 and the possible slip systems are randomly populated by dislocations, the contrast factors can be  
140 averaged over the permutations of the  $hkl$  indexes. In such cubic polycrystalline materials the  
141 average contrast factors are a function of a single parameter,  $\bar{C} = \bar{C}(q)$ .

142  
143 In the present martensitic alloy there are no planar defects, therefore we have described line  
144 broadening only by the size effect and dislocations. The size and strain profile functions are  
145 given by  $m$ ,  $\zeta$ ,  $\rho$ ,  $M$  and  $q$ . The asymmetric profiles require two size and two strain profiles. This  
146 means that the microstructure has been characterized by altogether 10 physical parameters. In  
147 order to improve the reliability of the evaluation, the CMWP software package has recently been  
148 amended [16]. The global minimum of the physical parameters is obtained by combining the  
149 Marquard-Levenberg nonlinear least-squares method and the Monte-Carlo fitting procedure [16].  
150 The improved CMWP applies the two procedures alternatingly, while, in the Monte-Carlo  
151 procedure, the relative searching range of the physical parameters decreases exponentially from  
152 about 0.4 to about 0.02. The quality of the fit has been measured by the goodness-of-fit,  $R^2$ ,

153 value. The CMWP evaluation was carried out for all diffraction peaks from 110 to 330  
154 simultaneously. A typical axial diffraction pattern for the  $\epsilon=0.03$  tensile deformed state is shown  
155 in Fig. 4a.

156  
157 To describe the strain part of asymmetric profiles we used the sum of two symmetric strain  
158 profile functions, each of which were shifted to smaller or larger  $d^*$  values around the center of  
159 gravity of the measured peaks. The robustness of the fitting procedure is shown in Fig. 4b. In  
160 order to see the difference between fitting with a single or two strain profiles only a section of  
161 the pattern is shown between  $d^*=6.5$  nm and  $d^*=11.7$  nm. Asymmetry concerns mainly the  
162 lower intensity parts of the profiles. In order to see the quality of fitting better, the intensity is in  
163 logarithmic scale. In the upper pattern two, whereas in the lower pattern only one strain profile  
164 has been used. In the upper measured (open circles) and fitted (red solid line) patterns the fitting  
165 is very good on both sides of the asymmetric profiles. Here  $R^2=0.9045$  has been obtained. In the  
166 lower measured (open circles) and fitted (red solid line) patterns the fitting is good on the right  
167 hand side, however, on the left hand side, especially in the lower intensity ranges, the measured  
168 data are well above the fitted curves indicating that the second peak is missing. Here  $R^2$  has been  
169 obtained to be  $R^2=0.782$ .

170  
171 In the initial state, all the diffraction peaks are almost perfectly symmetric within the  
172 experimental error. However, in the tensile deformed states, they become pronouncedly  
173 asymmetric, beyond the experimental error. This is illustrated for the 200 axial and side case  
174 diffraction peaks in Figs. 5a and 5b, respectively. The figures clearly show that after deformation  
175 the peaks become asymmetric and that the asymmetries in the axial and side case peaks occur in  
176 opposite directions. The tail parts of the asymmetric peaks are longer in the smaller or the larger  
177  $d^*$  directions in the axial or side cases, respectively. Here  $d^*=1/d$ , the reciprocal of the  $d$   
178 spacings in the crystal. The reversal of peak asymmetry is qualitatively similar to the  
179 characteristic peak asymmetry observed earlier in tensile deformed copper single [11-13] or  
180 polycrystals [17-20] with dislocation cell structures. This type of peak asymmetry is evidence for  
181 the composite behavior in heterogeneous microstructures, especially in heterogeneous  
182 dislocation distributions.

183

184 The evaluation of the sub-peak shifts,  $\Delta d^*$ , is shown in Fig. 5c and 5d for two typical 200 axial  
185 and side case profiles. The  $hkl$  dependent local strains,  $\epsilon_{hkl}=(\Delta d/d)_{hkl}$ , have been evaluated from  
186 the sub-peak shifts,  $\Delta d^*$ , and are shown for the 200, 211, 220 and 310 reflections in Fig. 6a as a  
187 function of true strain. The figure indicates that the absolute values of  $\epsilon_{hkl}$  for the 200 and 310  
188 reflections are systematically larger than the shifts of the 211 and 220 sub-peaks. This effect is  
189 due to elastic anisotropy. The  $hkl$  dependent local long-range internal stresses,  $\Delta\sigma_{hkl}$ , have been  
190 calculated as:  $\Delta\sigma_{hkl}=E_{hkl}\Delta\epsilon_{hkl}$ , where  $E_{hkl}$  are the  $hkl$  dependent Young's modules. The  $E_{hkl}$  values  
191 have been determined in [10] from the elastic parts of the lattice strain measurements for the  
192 same specimen investigated here also. The measured values are:  $E_{100}=167(\pm 2)$  GPa,  
193  $E_{110}=229(\pm 3)$  GPa,  $E_{211}=223(\pm 3)$  GPa and  $E_{310}=183(\pm 3)$  GPa. The  $\Delta\sigma_{hkl}$  values are plotted as a  
194 function of the true stress in Fig. 6b. The figure indicates that these values reveal a much weaker  
195  $hkl$  dependence than the  $\epsilon_{hkl}$  values. This result suggests that the behavior of the long-range  
196 internal stresses conforms more to the Taylor [20] than to the Sachs [21] model of plasticity.  
197 Both,  $\epsilon_{hkl}$  and  $\Delta\sigma_{hkl}$  have been evaluated also from the asymmetric side-case profiles. The values  
198 were obtained to be smaller than from the axial-case profiles by a factor of Poisson's number, i.e  
199 by about a factor of 0.33.

200

201 The two shifted sub-profiles have been evaluated for the average dislocation densities in the HO  
202 and SO packet components. The results are shown as a function of strain in Fig. 7a. The integral  
203 intensity ratio of the sub-profiles corresponding to the HO and SO packets provided the volume  
204 fractions of the two components,  $f_{HO}$  and  $f_{SO}$ . We will denote the stresses acting in the tensile and  
205 shear directions by  $\sigma$  and  $\tau$ . The two stresses are coupled by the Taylor factor,  $M_T$ :  $\sigma=M_T\tau$  [20].  
206 The average flow stress values,  $\sigma_{av}$  or  $\tau_{av}$ , and the local flow stress values,  $\sigma_{HO}$  or  $\tau_{HO}$  and  $\sigma_{SO}$  or  
207  $\tau_{SO}$ , acting in the HO and SO packets, have been calculated by the Taylor equation [23]:

208

$$209 \quad \sigma_i = \sigma_0 + \alpha G M_T b \sqrt{\rho_i}, \quad (1a)$$

210

$$211 \quad \tau_i = \tau_0 + \alpha G b \sqrt{\rho_i}, \quad (1b)$$

212

213 where  $i$  stands for, HO or SO,  $\alpha$  is a free parameter usually between zero and 1,  $G$  is the shear  
 214 modulus,  $b$  is the absolute value of the Burgers vector and  $\rho_i$  is the total or the local average  
 215 dislocation density, latter either in the hard, HO, or soft, SO, packets, respectively. Throughout  
 216 this work all local parameter values are average values for all the grains within the illuminated  
 217 volume of the polycrystalline specimen. Rietveld refinement has been done allowing for the two  
 218 phases, i.e. the HO and SO fractions of the packets. The details of this analysis are given in [10].  
 219 Rietveld analysis did provide the same average lattice parameter values for the two components  
 220 as the ones one could obtain from the peak shifts determined here.

221  
 222

#### 223 4. Evolution of the dislocation density and structure in HO and SO martensite lath-packets

224

225 During plastic deformation, dislocations are created and annihilated at the rates of creation,  $\dot{\rho}_{cr}$ ,  
 226 and annihilation,  $\dot{\rho}_{anni}$ . In work hardening the creation rate exceeds the annihilation rate,  
 227  $\dot{\rho}_{cr} > \dot{\rho}_{anni}$ , and the total dislocation density increases,  $\dot{\rho}_{tot} > 0$ . At large deformations the rate  
 228 of annihilation can increase to match the rate of creation,  $\dot{\rho}_{cr} = \dot{\rho}_{anni}$ , and the total dislocation  
 229 density will reach a saturation value,  $\rho_{tot} = \rho_{sat}$ , where  $\dot{\rho}_{tot} = 0$ . In Ref. [24] it was shown that if,  
 230 for any reason, the starting dislocation density is larger than the saturation value, i.e.  $\rho_{ini} > \rho_{sat}$ , the  
 231 annihilation rate will exceed the rate of creation,  $\dot{\rho}_{anni} > \dot{\rho}_{cr}$ . Under these conditions the total  
 232 dislocation density will decrease even during plastic deformation,  $\dot{\rho}_{tot} < 0$ . In such a case work  
 233 softening can be observed.

234

235 In lath martensites the initial dislocation density,  $\rho_{ini}$ , is created by martensitic transformation.  
 236 The process produces very large dislocation densities of the order of  $10^{16} \text{ m}^{-2}$  [3,25]. In Ref. [24]  
 237 it was shown that work hardening or softening depends on the relation between the initial,  $\rho_{ini}$ ,  
 238 and the saturation values,  $\rho_{sat}$ , of the dislocation densities. The two processes are uniformly  
 239 described by equation (6) in Ref. [24]:

240

$$241 \quad \rho(\gamma) = [(\rho_{sat})^{1/2} - \beta \exp(-\frac{\gamma^* \gamma}{2b})]^2, \quad (2)$$

242

243 where  $\gamma$  is the shear deformation,  $\beta=(\sqrt{\rho_{sat}} - \sqrt{\rho_{ini}})$ ,  $y^*$  is the effective annihilation distance of  
 244 dislocations as defined in Refs. [24], [26] and [27] and  $\gamma=2\varepsilon$ ,  $\varepsilon$  being the deformation in the  
 245 tensile direction. We shall interpret only the ratio of the annihilation distance in the soft and hard  
 246 components of the deformed lath-martensite,  $y_{SO}^*/y_{HO}^*$ . The interpretation of the annihilation  
 247 distance,  $y^*$  itself, is not an essential issue, since in equation (2) it is only a fitting parameter.  
 248 Based on the Orowan equation [28] it can be assumed that the mean free path of dislocations,  $\Lambda$ ,  
 249 scales with the average dislocation distance,  $\Lambda=h'/\sqrt{\rho}$ , where  $h'$  is the scaling factor. In Refs.  
 250 [26,27] it was shown that at saturation the annihilation distance also scales with the saturation  
 251 value of the dislocation distance:  $y^*=h''/\sqrt{\rho_{sat}}$ , where  $h''$  is the scaling factor. Since both,  $y^*$  and  
 252  $\Lambda_{sat}$  scale with  $1/\sqrt{\rho_{sat}}$ , the ratios of the two quantities in the SO and HO components of the  
 253 deformed lath martensite are equal at saturation:

254

$$255 \quad y_{SO}^*/y_{HO}^* = \Lambda_{sat}^{SO}/\Lambda_{sat}^{HO} \cong 50 . \quad (3)$$

256

257 The dislocation density values at saturation,  $\rho_{sat}$  and the signed values of  $\beta$  in the SO and HO  
 258 components, as obtained from equation (2), are listed in Table 1. When  $\beta$  is positive or negative,  
 259 the rate of dislocation annihilation is smaller or larger than the rate of dislocation creation,  
 260 respectively [24]. The former case corresponds to work hardening and the latter to work  
 261 softening.

262

263 In the packets where the active dislocations (i.e. the dislocations with the largest Schmid factor)  
 264 move along the lath planes, the mean free paths,  $\Lambda$ , and the effective annihilation distances,  $y^*$ ,  
 265 will be relatively long. When, however, the active dislocations cross the lath-plane boundaries  
 266 both the mean free paths,  $\Lambda$ , and the effective annihilation distances,  $y^*$ , will be relatively short.  
 267 In the first case, the lath-packets will soften, whereas in the second case they will harden,  
 268 producing soft and hard packets with composite behavior. Softening and hardening disrupts the  
 269 dislocation distribution which was homogeneous on the scale of lath dimensions in the as  
 270 quenched initial state. In the SO and HO components the dislocation densities decrease or  
 271 increase relative to the initial average value, and vary spatially on the length scale of martensite  
 272 packets. Load is redistributed between SO and HO martensite packets in correlation with the

273 composite behavior. Dislocation dynamics simulations in fcc crystals, see Ref. [29], have shown  
274 that the mean free path of dislocations play a key role in strain hardening. The present work  
275 indicates that  $\Lambda$  along with  $y^*$  are key quantities in strain softening or hardening, which is in  
276 good correlation with [29].

277  
278 Screw or edge type dislocations have different diffraction contrast [30]. The CMWP procedure  
279 takes into account strain anisotropy and also provides the average fraction values of edge and  
280 screw type dislocations [14,15]. The analysis provided that in the SO packets the dislocations are  
281 mainly of screw character, which does not change during plastic deformation. In the HO  
282 components, however, the dislocation character changes gradually from screw to edge character  
283 as a function of plastic strain, as indicated in Table 1. Screw dislocations can move in any  
284 direction therefore annihilate relatively easily even when they are farther apart from each other.  
285 Edge dislocations, however, will either glide on slip planes or climb when annihilating, so can  
286 only annihilate when they are close to each other. The relatively large ratios between the  
287 effective annihilation distances and mean free paths in the SO and HO packets, see in eq. (3),  
288 correlate well with the different dislocation characters in these packets. Further details on how  
289 dislocation character changes with plastic deformation will be given in Ref. [10].

290  
291 The total average dislocation density,  $\rho_t$ , was calculated from the two local values as the  
292 weighted average,  $\rho_t = f_{HO}\rho_{HO} + (1 - f_{HO})\rho_{SO}$ , where  $f_{HO}$  is the volume fraction of the HO  
293 component. The volume fraction,  $f$ , of the HO fraction has been found to vary around  
294  $f = 0.48 \pm 0.05$ , right from the beginning of plastic deformation and it did not change within the  
295 investigated deformation range. The flow stress values,  $\sigma_i$ , calculated by equation (1) are shown  
296 in Fig. 7b vs. the measured applied stress,  $\sigma_{applied}$ . In equation (1),  $\alpha$  was allowed to vary with  
297 deformation in the HO oriented packets as it is shown in Fig. 7c.

298  
299 The value of  $\alpha$  is usually considered a constant, but in the HO packets we must have an  $\alpha$  with a  
300 changing value. Unless we have a changing  $\alpha$  value, the increase of dislocation density alone  
301 would be totally insufficient to account for the increase in the flow stress. A number of  
302 experimental results have shown that the value of  $\alpha$  changes with dislocation arrangements  
303 during plastic deformation [31-35]. In the SO packets the dislocation density decreases at the

304 beginning of plastic deformation and then stays constant. Since here neither the dislocation  
 305 density nor its arrangement changes considerably, the value of  $\alpha$  is a constant. The local flow  
 306 stresses,  $\sigma_{HO}$  and  $\sigma_{SO}$  in the HO and SO packets indicate that the moment plastic deformation  
 307 starts, stress is redistributed between the two packet types, see Fig. 7b. Compared to the applied  
 308 stress values, the local flow stress decreases in the SO packets, but increases in the HO packets.  
 309 The  $\sigma_{initial}$  value is the flow stress corresponding to the initial average dislocation density:  
 310  $\sigma_{initial} = \sigma_0 + \alpha G M_T b \sqrt{\rho_{initial}}$ , where  $\sigma_0$  is the friction stress of the alloy.

311

312

### 313 5. Composite model of plastically deformed lath-martensite

314

315 The shifts,  $\Delta d^*$ , are evaluated in terms of residual internal stresses,  $\Delta\sigma$ , corresponding to the  
 316 forward and backward stresses which act in the hard-orientation (HO) or soft-orientation (SO)  
 317 packets. The two different packet orientations, HO and SO, are those in which the active Burgers  
 318 vectors are out-of-lath-plane and in-lath-plane.

319

320 The microscopic model of stress redistribution is based on the composite model of Mughrabi  
 321 [11-13] and is shown schematically in Fig. 8. In the initial state, the microstructures are identical  
 322 in the packets with different orientations. Fig. 8a shows three adjacent packets with identical  
 323 dislocation structures. Two packets have vertical and one has horizontal laths. In the central  
 324 packet the active Burgers vector is parallel to the lath plane directions, whereas in the other two  
 325 they cross the lath boundaries. As schematically shown in Fig. 8b, the central SO packet will  
 326 soften during plastic deformation whereas the HO packets will harden. After unloading, forward  
 327 and backward residual stresses will remain in the HO and SO packets, respectively. Stress and  
 328 strain compatibility between the SO and HO packets is guaranteed by the geometrically  
 329 necessary dislocations (GNDs). They are lined up along the interfaces of the differently oriented  
 330 packets shown in Fig. 8c. The forward and backward local residual stresses are shown in Fig. 8d.  
 331 During loading the weighted averages of the local stresses add up to the applied stress [11]:

332

$$333 \tau_{applied} = f_{HO}\tau_{HO} + (1-f_{HO})\tau_{SO} . \quad (4)$$

334

335 After unloading the residual internal stresses in the HO and SO packets are:

336

337  $\Delta\tau_{HO}=\tau_{HO}-\tau_{applied}$  ,  $\Delta\tau_{SO}=\tau_{SO}-\tau_{applied}$  , where  $f_{HO}\Delta\tau_{HO} + (1-f_{HO})\Delta\tau_{SO} = 0$ . (5)

338

339 In the composite model of plastic deformation of heterogeneous microstructures,  $\Delta\tau_{HO}$  and  $\Delta\tau_{SO}$   
340 are called 'long range internal stresses' [11-13]. During plastic deformation, the backward  
341 stresses in the SO and the forward stresses in the HO packets will either hamper or assist  
342 dislocation motion so as to make the entire material flow simultaneously. The backward and  
343 forward stresses ensure that macroscopic flow takes place irrespective of the packets being soft  
344 or hard. In the HO packets the dislocation character gradually changes from screw to edge type  
345 when plastic deformation takes place. This change in dislocation character causes the  
346 annihilation distance to decrease, which in turn contributes to the increase of dislocation density.  
347 Statistical fluctuations are not taken into account in the simple schematic model of long range  
348 internal stresses, see Fig. 8d. No doubt the magnitude of long range internal stresses varies  
349 statistically as has been shown in several high resolution X-ray diffraction experiments [17-20].  
350 The local variation and fine details of the long range internal stresses requires similar high  
351 resolution X-ray diffraction experiments as in the case of plastically deformed copper crystals  
352 [17-20]. The strengthening effect of retained austenite has not been discussed here, but further  
353 details will be given in [10]. In the present alloy the volume fraction of retained austenite is  
354 about 3.7%. As it will be discussed in [10], this amount contributes to the average strength of the  
355 material. However, the contribution is less than about 9%, and has practically no effect on the  
356 long range internal stresses or the composite behavior described and discussed here.

357

358

## 359 **Conclusions**

360

361 Based on high-resolution neutron diffraction experiments we have shown that the initially  
362 homogeneous dislocation structure in lath-martensite is disrupted by tensile deformation. Packets  
363 with active Burgers vectors having either in-lath-plane or out-of-lath-plane orientation, will  
364 soften or harden as a function of plastic deformation. The dislocation densities will become  
365 smaller or larger than the initial average value in the softening or hardening packets. Plastic

366 deformation produces a heterogeneous microstructure consisting of soft and hard martensite  
367 packets, and the material, thus consisting of two components, behaves like a composite. Long  
368 range internal stresses are being formed, and they act backward or forward in the soft and hard  
369 components. Load is redistributed between the soft and hard components. The backward and  
370 forward stresses hamper or assist dislocation movement in the soft or hard components. As a  
371 result, both components undergo plastic deformation simultaneously. In order to understand the  
372 relatively ductile and high strength nature of lath-martensite steels, one has to take into account  
373 that the initially homogeneous microstructure will turn into a composite as a result of plastic  
374 deformation.

375

376

### 377 **Acknowledgements**

378

379 The authors are grateful to the Japan Society for the Promotion of Science Grant-in-Aid for  
380 Scientific Research for partial support under grant No. 26289264. T.U. and G.R are grateful for  
381 the partial support of the French State through the program "Investment in the future" operated  
382 by the National Research Agency (ANR) and referenced by ANR-11-LABX-0008-01, LabEx-  
383 DAMAS. The authors thank the Education Commission of Hubei Province of China (No.  
384 B20161203), for the specimen. The neutron diffraction experiments were conducted at the  
385 Materials and Life Science Experimental Facility of J-PARC with the proposals of 201410019.

386

387

388

389 **References**

390

- 391 1. G. Krauss, *Mater. Sci. Eng.*, 1999, vol. A273–275, pp. 40-57.
- 392 2. G. Krauss, A. R. Mader, *Metallurgical Transactions.*, 1971, vol. 2, pp. 2343-2357.
- 393 3. S. Morito, H. Tanaka, R. Konishi, T. Furuhashi, T. Maki, *Acta Mater.*, 2003, 51, pp. 1789-  
394 1799.
- 395 4. H. Kitahara, R. Ueji, N. Tsuji, Y. Minamino, *Acta Mater.*, 2006, vol. 54, pp. 1279–1288.
- 396 5. T. Swarr, G. Krauss, *Metall. Transact.*, 1976, vol. 7A, pp. 41-48.
- 397 6. M. Michiuchi, S. Nambu, Y. Ishimoto, J. Inoue, T. Koseki, *Acta Mater.*, 2009, vol. 57,  
398 pp. 5283-5291.
- 399 7. S. Nambu, M. Michiuchi, Y. Ishimoto, K. Asakura, J. Inoue, T. Koseki, *Scripta Mater.*,  
400 2009, vol. 60, pp. 221–224.
- 401 8. H. Ghassemi-Armaki, P. Chen, S. Bhat, S. Sadagopan, S. Kumar, A. Bower, *Acta Mater.*  
402 61 (2013) 640–3652.
- 403 9. Y. Mine, K. Hirashita, H. Takashima, M. Matsuda, K. Takashima, *Mater. Sci. Eng.*,  
404 2013, vol. A560, pp. 535–544.
- 405 10. S. Harjo, T. Kawasaki, Y. Tomota, W. Gong, K. Aizawa, Z. Shi, G. Ribárik, T. Ungár, to  
406 be submitted to *Int. J. Plasticity*.
- 407 11. H. Mughrabi, *Acta Metall.*, 1983, vol. 31, pp. 1367-1379.
- 408 12. T. Ungár, H. Mughrabi, D. Rönnpágel, M. Wilkens, *Acta Metall.*, 1984, vol. 32, pp. 333-  
409 342.
- 410 13. H. Mughrabi, T. Ungár, W. Kienle, M. Wilkens, *Philos. Mag.*, 1986, vol. A53, pp. 793-  
411 813.
- 412 14. G. Ribárik, T. Ungár, *Mater. Sci. Eng.*, 2010, vol. A528, pp. 112–121.
- 413 15. T. Ungár, L. Balogh, G. Ribárik, *Metall. Mater. Trans.*, 2010, vol. A41, pp. 1202-1209.
- 414 16. G. Ribárik, B. Jóni, T. Ungár, *in preparation*.
- 415 17. B. Jakobsen, H. F. Poulsen, U. Lienert, J. Almer, S. D. Shastri, H. O. Sørensen, C.  
416 Gundlach, W. Pantleon, *Science*, 2006, vol. 312, pp. 889–892.
- 417 18. L. E. Levine, B. C. Larson, W. Yang, M. E. Kassner, J. Z. Tischler, M. A. Delos-Reyes,  
418 R. J. Fields, W. Liu, *Nature Materials*, 2006, vol. 5, pp. 619–622.
- 419 19. H. Mughrabi, T. Ungár, *Nature Materials*, 2006, vol. 5, pp. 601–602.

- 420 20. B. Jakobsen, H. F. Poulsen, U. Lienert, W. Pantleon, *Acta Mater.*, 2007, vol. 55, pp.  
421 3421-3430.
- 422 21. G. I. Taylor, *J. Inst. Metals*, 1938, vol. 62, pp. 307-324.
- 423 22. G. Sachs, (1928). *Zeitschr. Verh. Deutsch. Ing.*, 1928, vol. 72, 734-736.
- 424 23. G. I. Taylor, *Proc. R. Soc. Lond.*, 1934, vol. A145, pp. 362-387.
- 425 24. T. Ungár, L. Li, G. Tichy, W. Pantleon, H. Choo, P. K. Liaw, *Scripta Mater.*, 2011, vol.  
426 64, pp. 876-879.
- 427 25. K. Nakashima, Y. Fujimora, H. Matsubayashi, T. Tsuchiyama, S. Takaki, *Tetsu-to-*  
428 *Hagane (in Japanese)*, 2007, vol. 93, pp. 459-465.
- 429 26. U. Essmann, M. Rapp, *Acta Metall.*, 1973, vol. 21, pp. 1305.
- 430 27. U. Essmann, H. Mughrabi, *Philos. Mag.*, 1979, vol. 40, pp. 731-756.
- 431 28. E. Orowan, *J. West Scotland. Iron Steel Inst.*, 1946, vol. 54, pp. 45-53.
- 432 29. B. Devincere, T. Hoc, L. Kubin, *Science*, 2008, vol. 320, pp. 1745-1748.
- 433 30. M. Wilkens, *phys. stat. sol. (a)*, 1970, vol. 2, pp. 359-370.
- 434 31. H. Mughrabi, *Mater. Sci. Eng.*, 1987, vol. A85, pp. 15-31.
- 435 32. E. Schafler, K. Simon, S. Bernstorff, P. Hanák G. Tichy, T. Ungár, M. J. Zehetbauer,  
436 *Acta Mater.*, 2005, vol. 53, pp. 315-322.
- 437 33. T. Ungár, A. D. Stoica, G. Tichy, X.-L. Wang, *Acta Mater.*, 2014 , vol. 66 pp. 251-261.
- 438 34. H. Mughrabi, *Current Opinions Sol. State Mater. Sci.* 2016, in the press.
- 439 35. B. P. J. Sandvik, C. M. Wayman, *Metall. Transac.*, 1983, vol. A14, pp. 809-822.
- 440
- 441
- 442

443 **Table 1.** The dislocation density values at saturation,  $\rho_{sat}$  as provided by equation (2), the signed  
444 values of  $\beta$  in the soft and hard components of the deformed lath martensite, as defined in  
445 equation (2) and the dislocation character of the majority of dislocations at saturation as provided  
446 by the CMWP procedure.

447

packets	$\rho_{sat}$ [ $10^{15} \text{ m}^{-2}$ ]	$\beta$ [1/nm]	dislocation character at saturation
SO	1.69 ( $\pm 0.1$ )	-0.71 ( $\pm 0.05$ )	screw
HO	18.7 ( $\pm 1$ )	2.27 ( $\pm 0.2$ )	edge

448

449

450

451

452

453

454 **Captions**

455

456 Figure 1.

457 Schematic illustration of the hierarchical structure of lath martensite with the active Burgers  
458 vectors. (a) Lath packets consisting of parallel blocks in three different packet. Each block  
459 consists of laths of two specific Kurdumov–Sachs [2] variant groups (sub-blocks) misoriented by  
460 small angles smaller than about 10 degrees. (b) Two packets oriented with the active Burgers  
461 vectors either in- or out-of-lath-plane relative to the direction of the applied stress,  $\sigma$ ,  
462 respectively.

463

464 Figure 2.

465 Schematic drawing of the in-situ neutron diffraction experiment. The specimen was mounted  
466 horizontally in a loading machine which was installed at the TAKUMI beamline, in such a way  
467 that the neutron diffraction patterns in the axial and axial directions were measured  
468 simultaneously using two detector banks at scattering angles of  $\pm 90^\circ$ .

469

470 Figure 3.

471 Stress-strain curve. Deformations in plastic regime were increased step by step followed by  
472 unloading at several strain values to improve counting statistics.

473

474 **Figure 4.**

475 (a) Typical diffraction pattern. The observed (open black-circles) and CMWP fitted (red line)  
476 neutron diffraction patterns for the  $\epsilon = 0.03$  tensile deformed state. The horizontal axis is the  
477 reciprocal of the d spacings, where  $d^* = 1/d$ . (b) A section of the measured (open black-circles)  
478 and CMWP fitted (red line) patterns. The upper patterns: with fitting two slightly shifted strain  
479 profiles into each peak profile in order to account for peak asymmetries. The lower patterns: with  
480 only one fitted strain profile into each peak profile. The letter A at the  $hkl$  indices indicates  
481 austenite reflections.

482

483 **Figure 5.**

484 Enlarged 200 diffraction profiles. The measured and CMWP calculated profiles for the  
485 undeformed (open triangles and blue lines) and  $\epsilon = 0.047$  tensile deformed (open squares and red  
486 lines) states in the axial (a) and axial (b) directions. (c) The CMWP calculated sub-profiles  
487 corresponding to the HO (dark green line) and the SO (blue line) packets in the axial direction,  
488 along with the measured data (open circles) and the CMWP calculated total profile (red line).  
489 The center of gravity of the measured profile and the positions of the sub-peaks are indicated as  
490 dotted, dashed and dash-dot lines, respectively. (d) The measured (open circle), the CMWP  
491 calculated total profile (red line) and the CMWP calculated sub-profiles corresponding to the HO  
492 (dark green line) and the SO (blue line) packets in the axial direction.

493

494 **Figure 6.**

495 (a) The relative shifts,  $\Delta d/d$ , of the sub-peaks obtained from the asymmetric axial case profiles as  
496 a function of true strain for the 200, 220, 311 and 222 reflections. (b) The long-range internal  
497 stress values,  $\Delta\sigma$ , as a function of true strain for the 200, 220, 311 and 222 reflections. The  
498 vertical thick black lines indicate the experimental error.

499

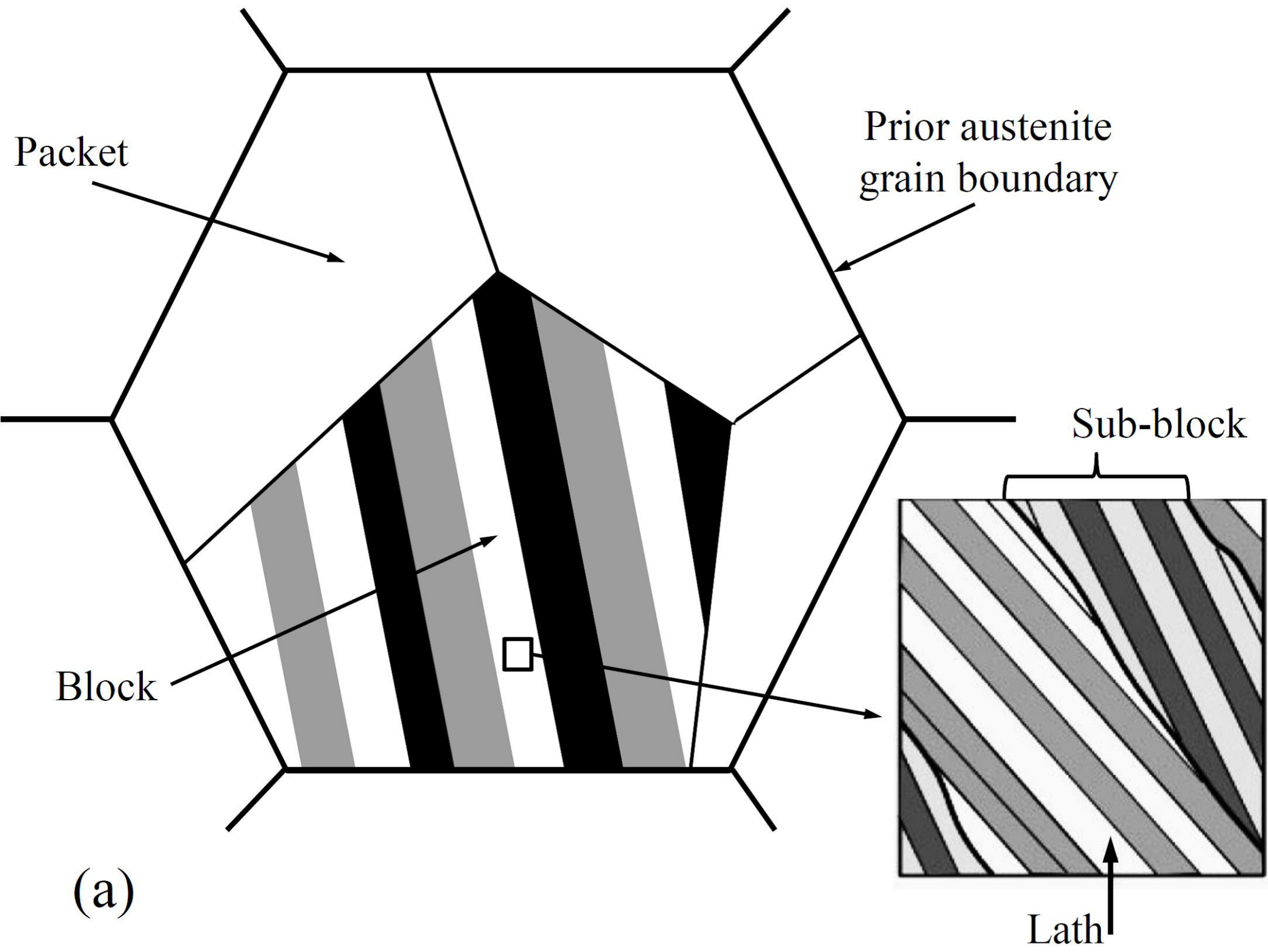
500 **Figure 7.**

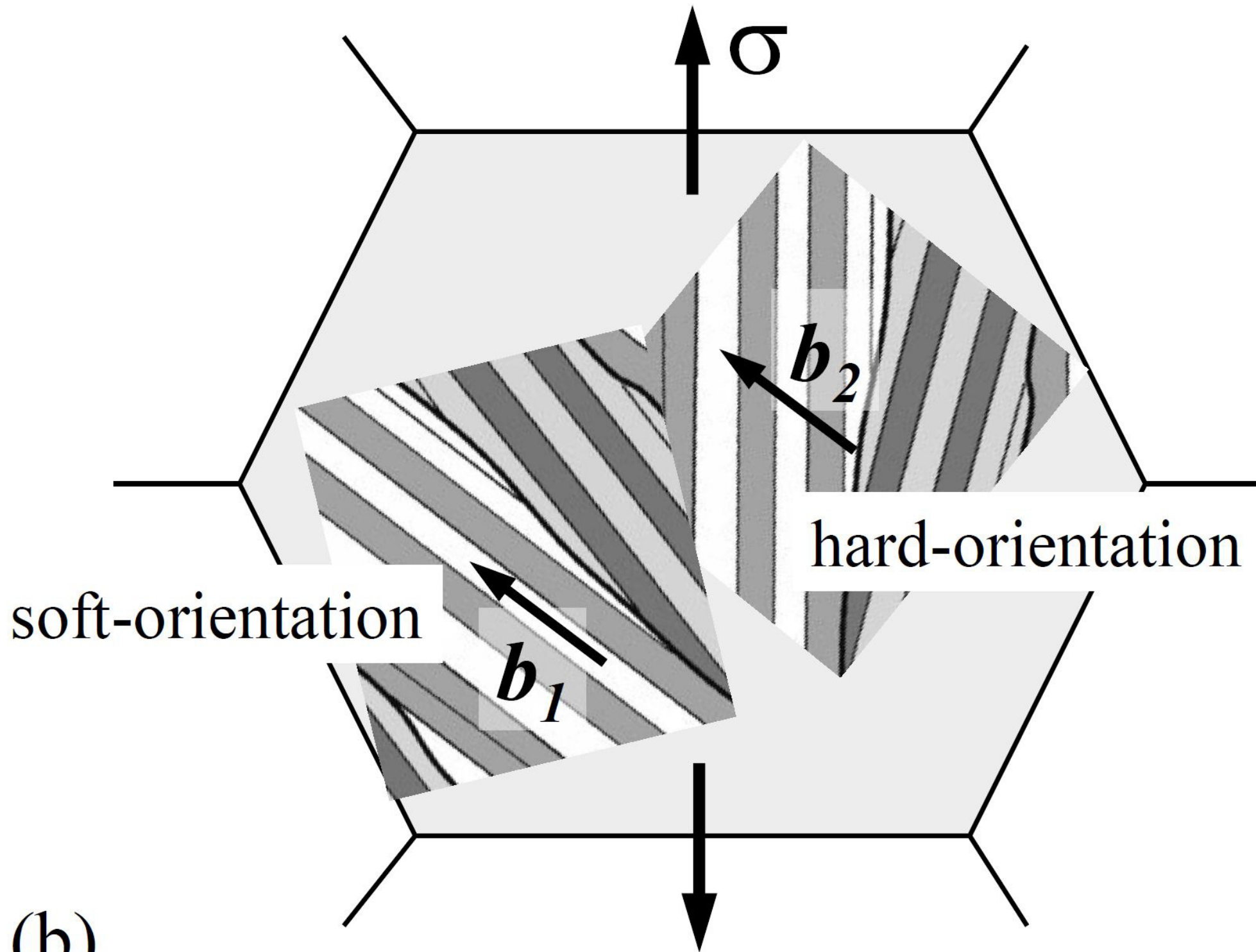
501 Dislocation density, stress partitioning and  $\alpha$  parameter in the Taylor equation. (a) Dislocation  
502 densities in the HO (red symbols) and the SO packets (blue symbols), and the volume fraction  
503 weighted average dislocation densities (black symbols). (b) Local stresses in the HO (red  
504 symbols) and the SO packets (blue symbols) calculated from the dislocation densities according  
505 to the Taylor equation in eq. (1). (c) The  $\alpha$  parameter in Taylor's equation calculated from the  
506 dislocation densities and the local stresses.

507

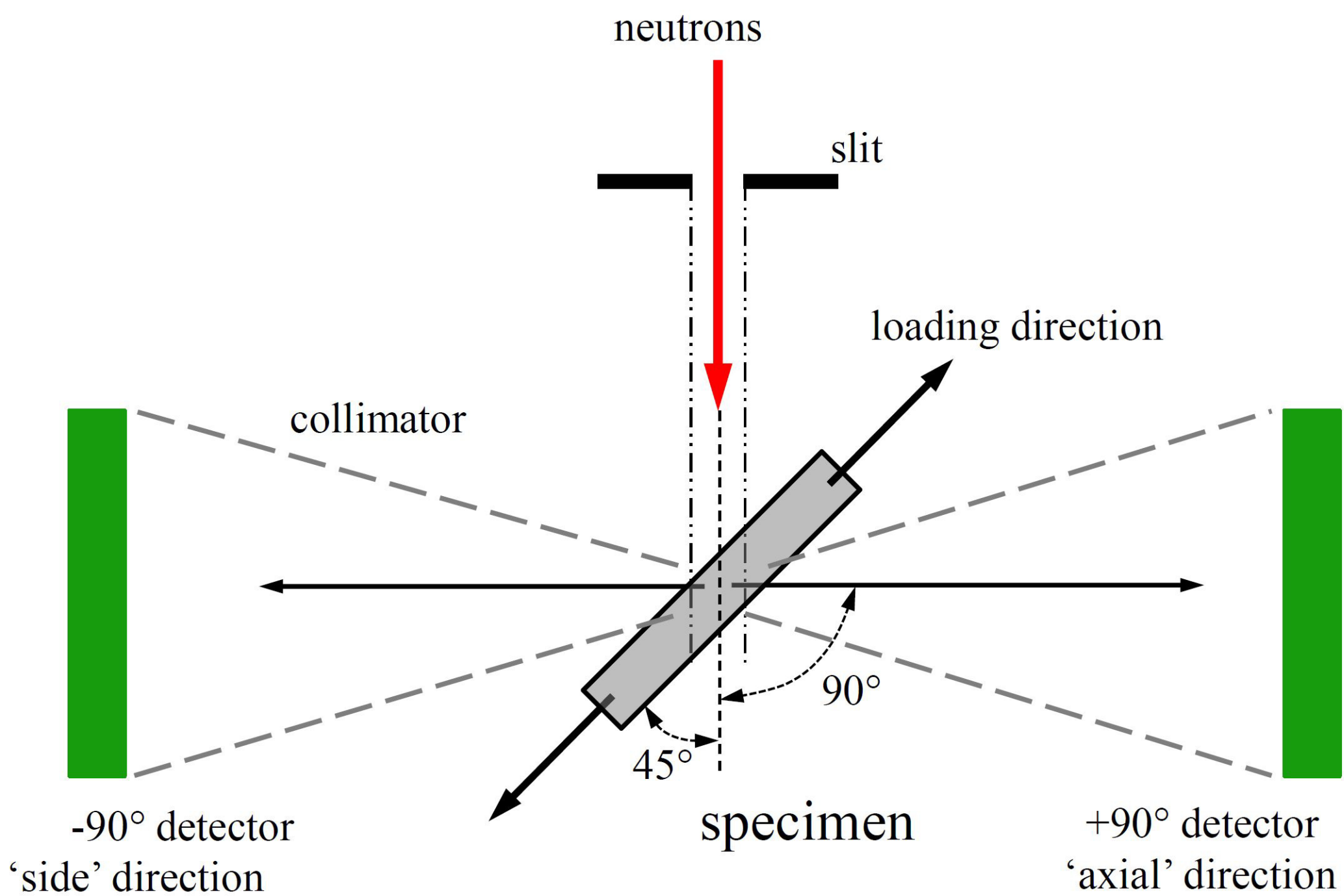
508 **Figure 8.**

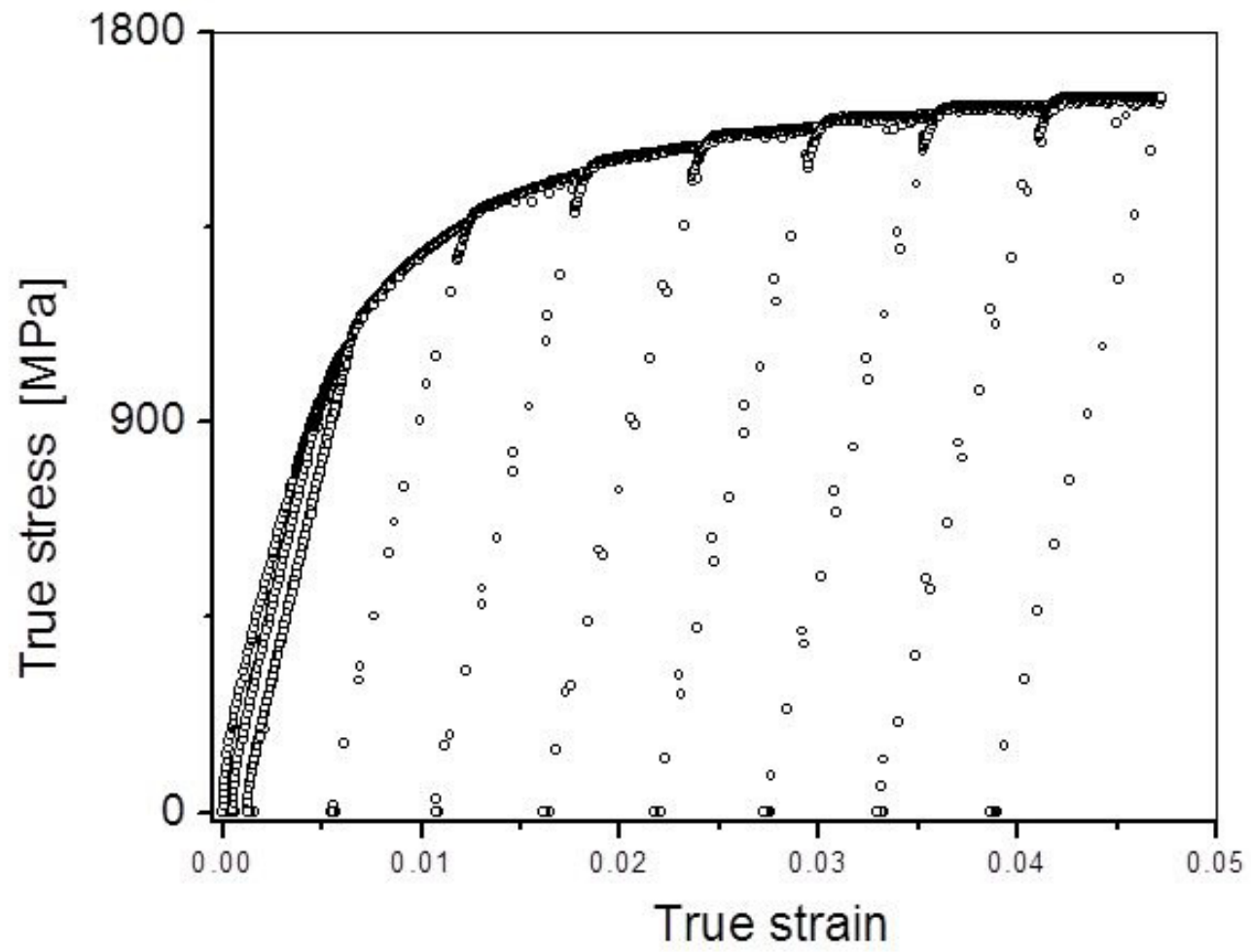
509 Schematic drawing of the composite model of the SO and HO packets in lath martensite. (a)  
510 Schematic arrangement of laths in different packets. The parallel laths are indicated by different  
511 parallel gray-scales. (b) Active Burgers vectors relative to the direction of the shear stress,  $\tau$ , in  
512 the HO and SO packets. (c) Schematic illustration of the GNDs lined up along the interfaces of  
513 the differently oriented packets. (d) Spatial distribution of the local long-range-internal-stresses  
514 in the HO and SO packets under the action of the applied stress.



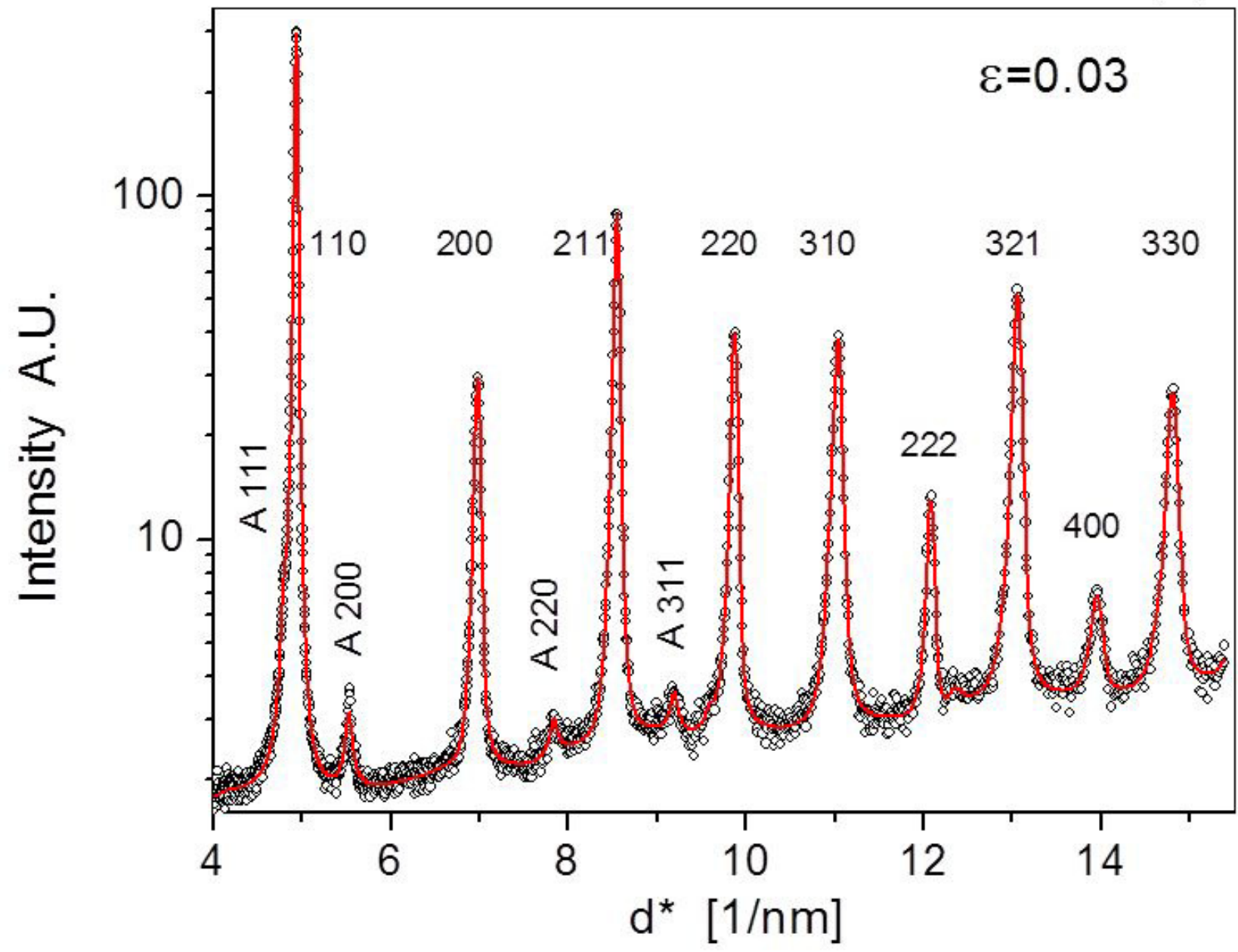


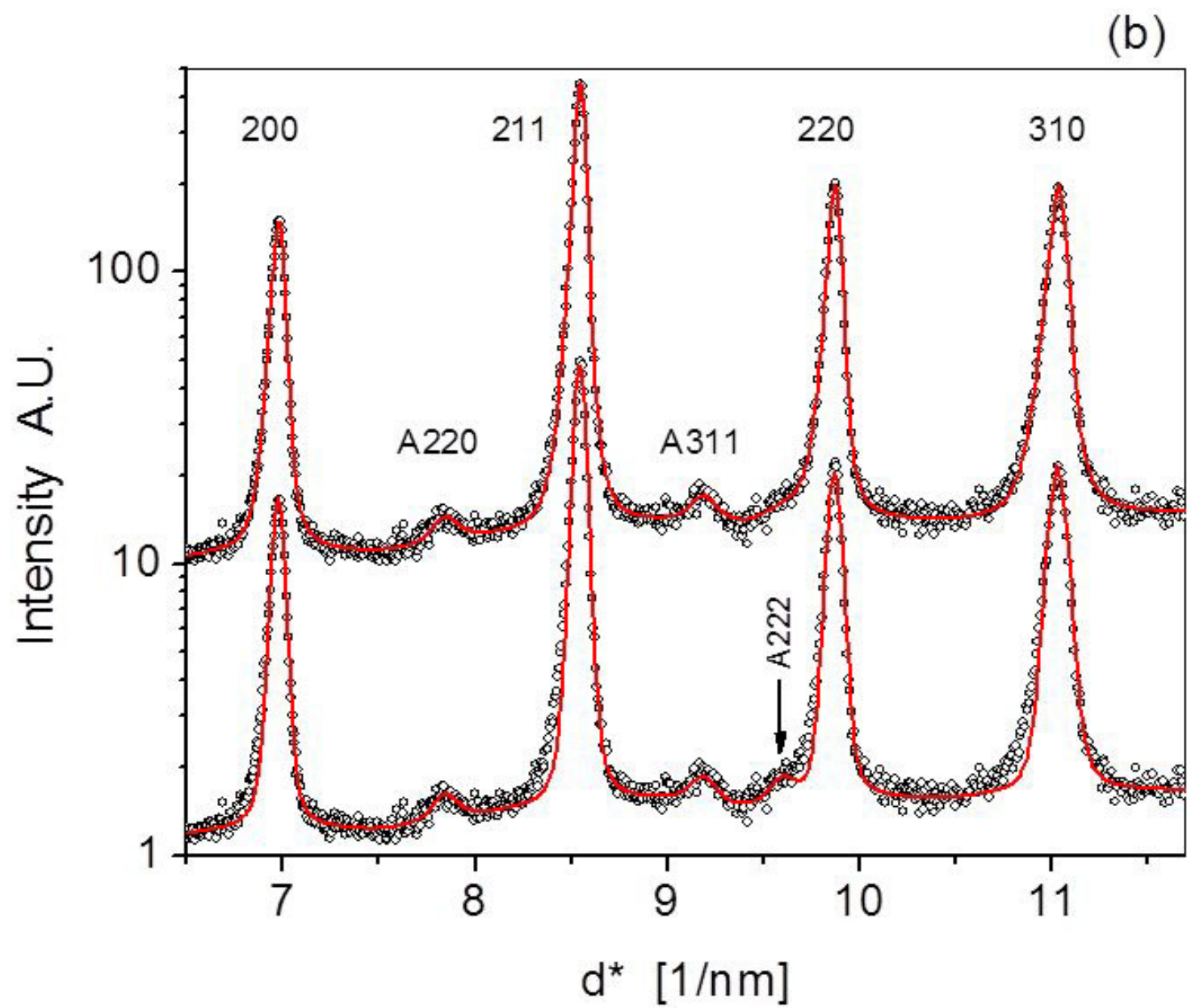
(b)



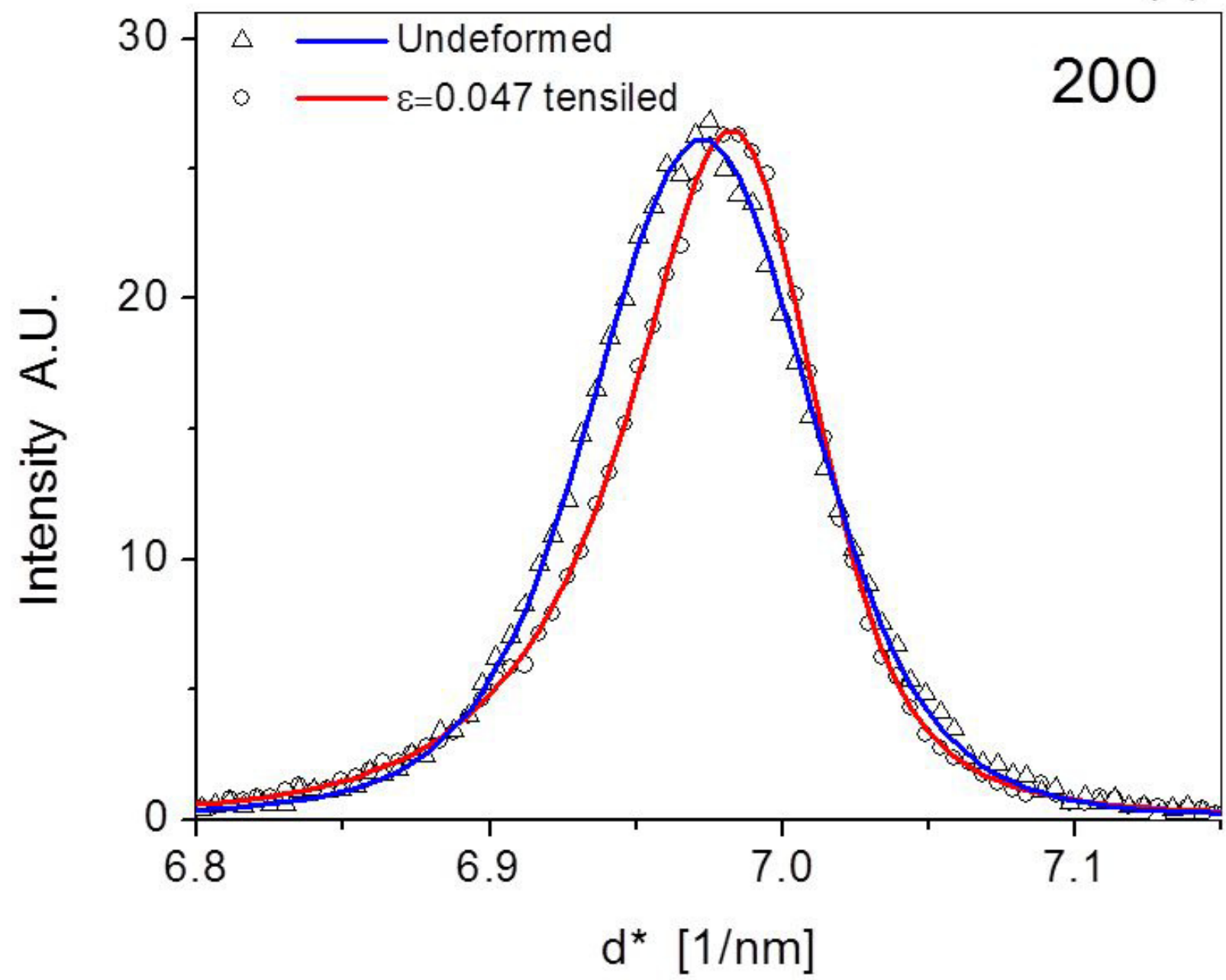


(a)

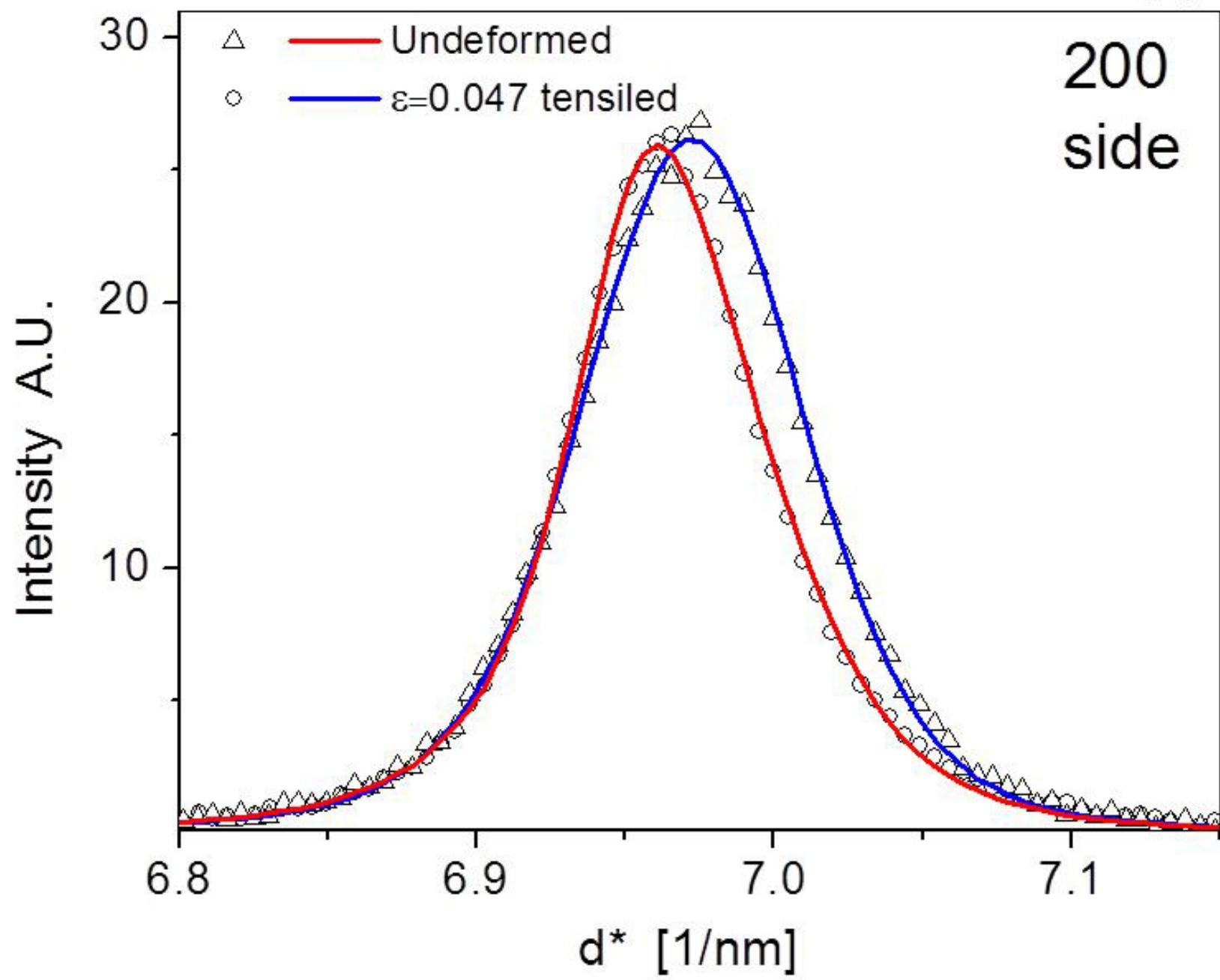




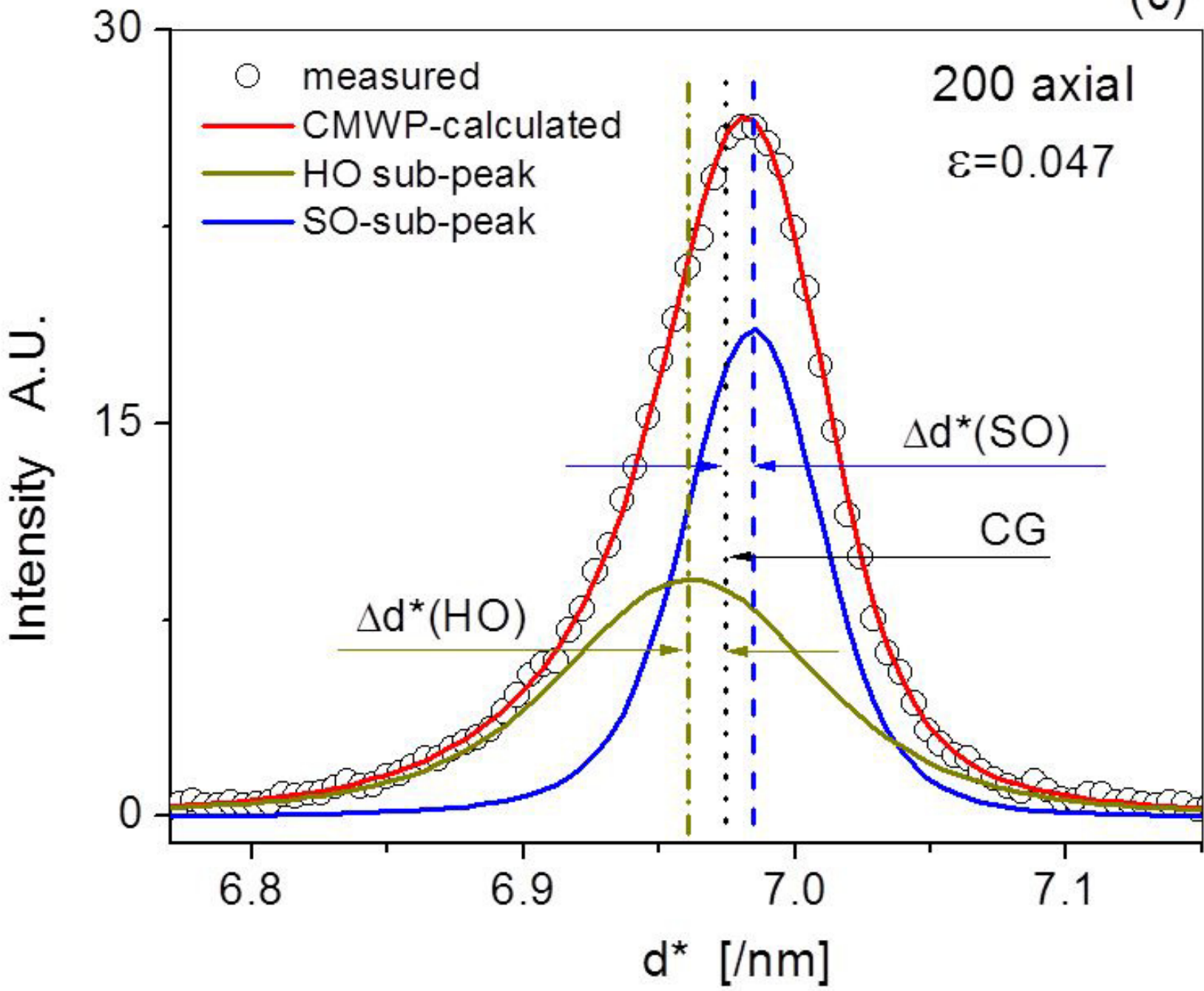
(a)



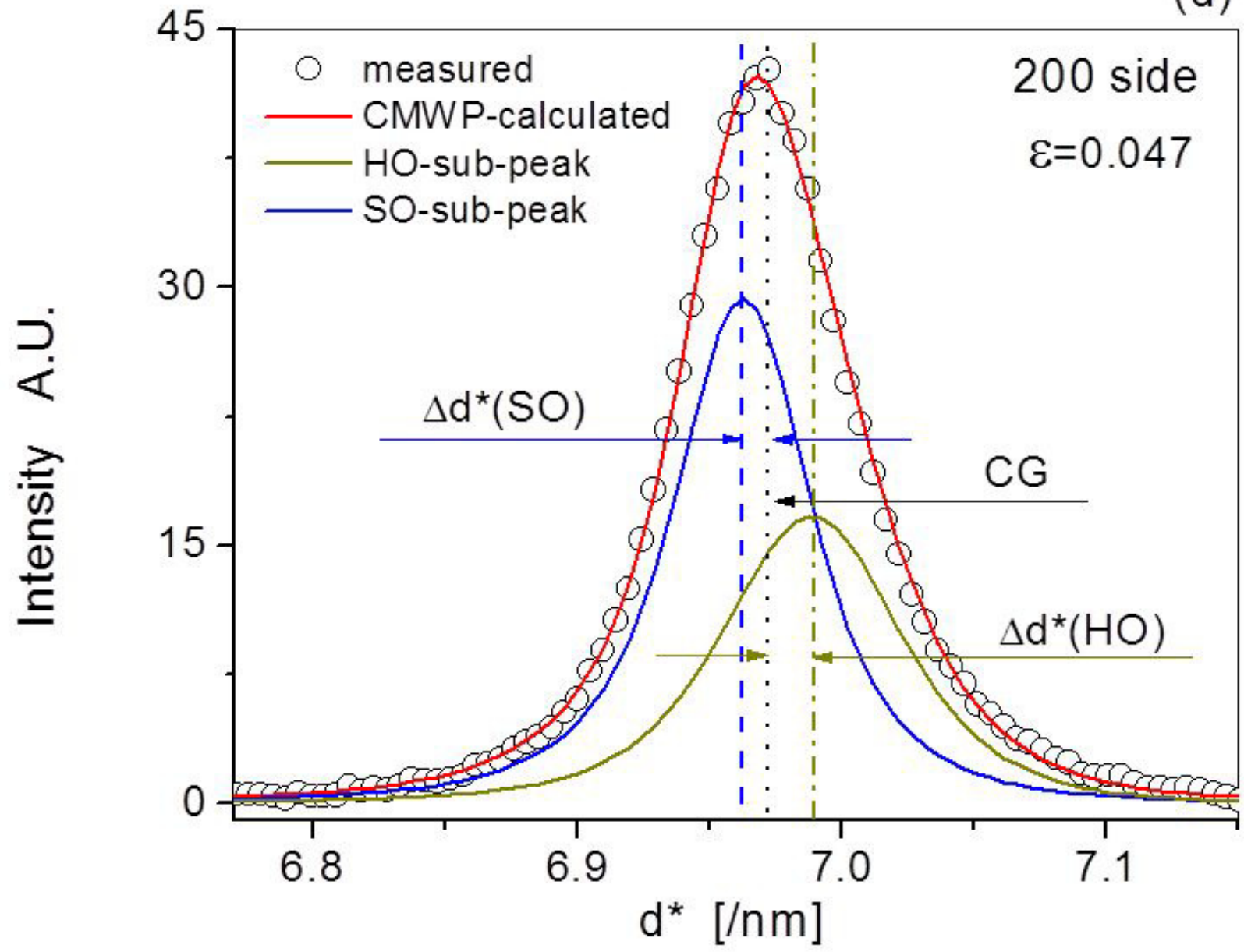
(b)

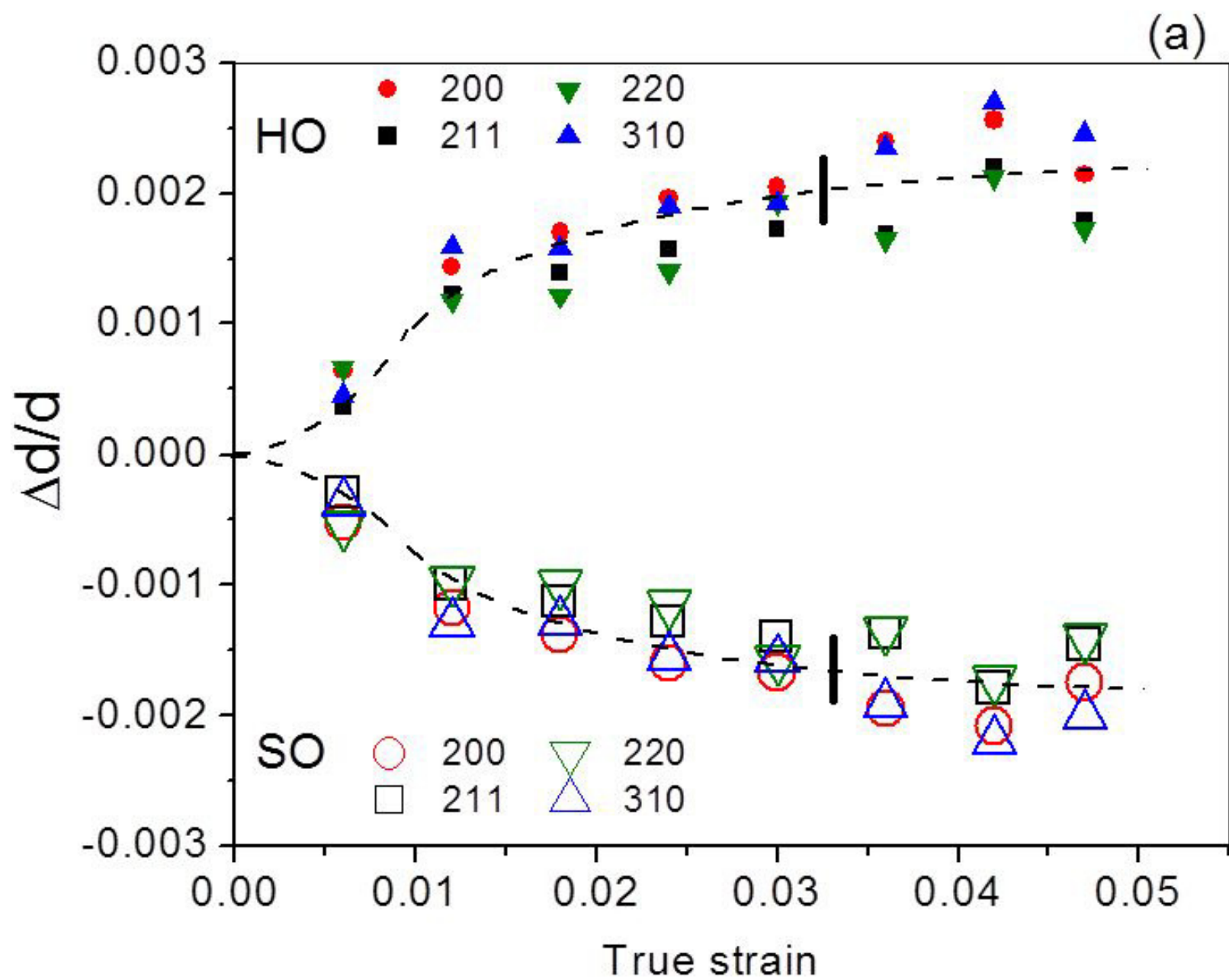


(c)

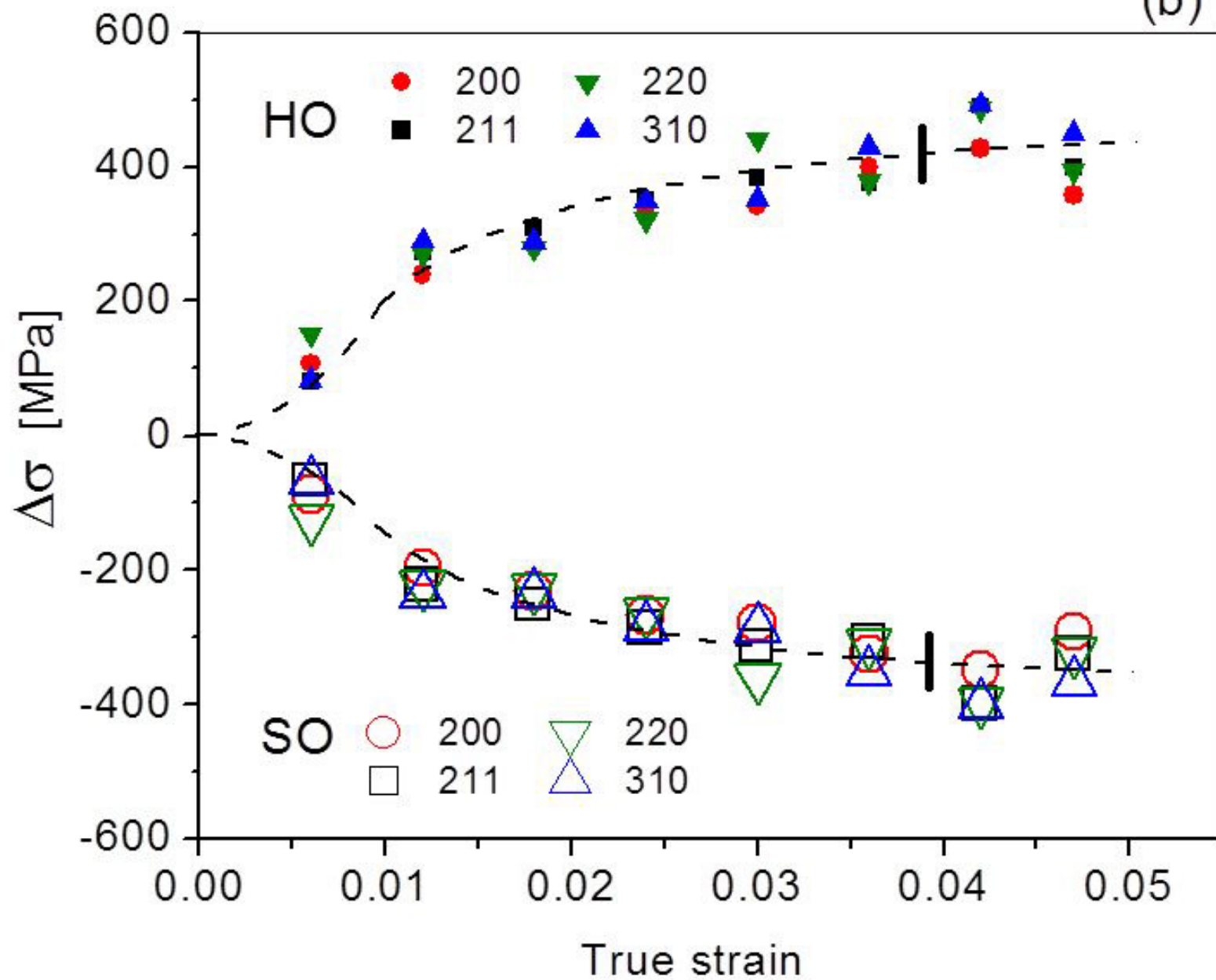


(d)

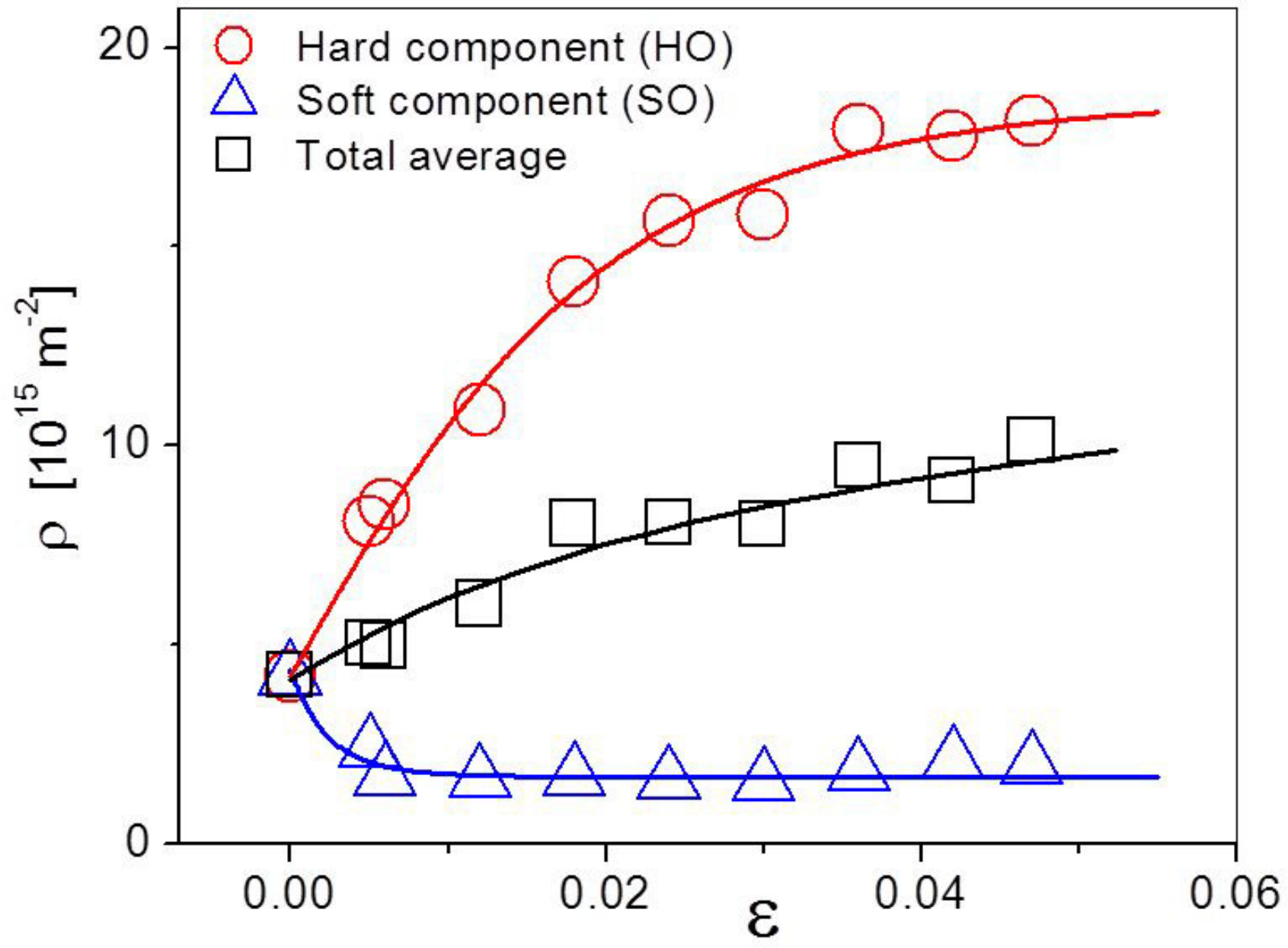


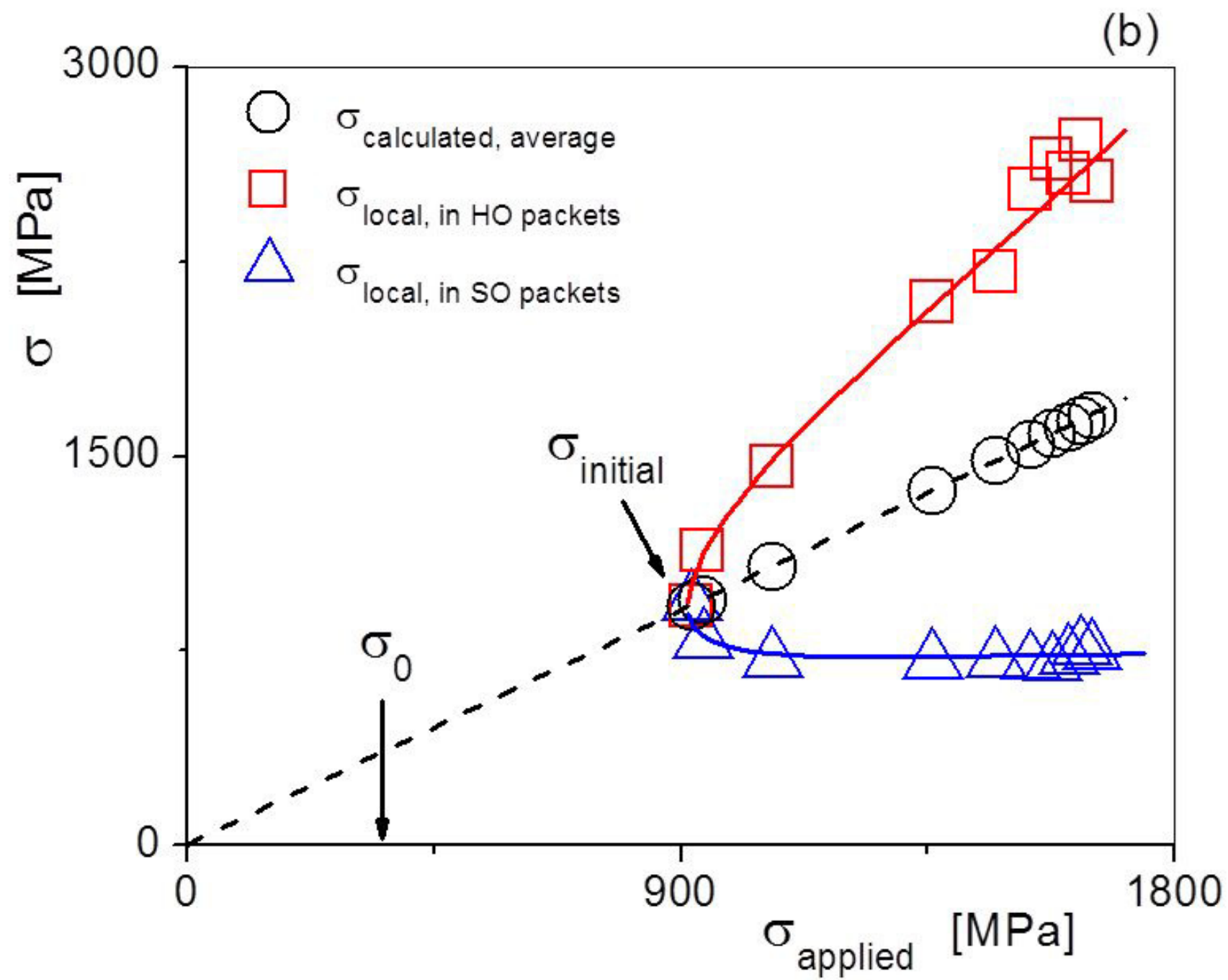


(b)

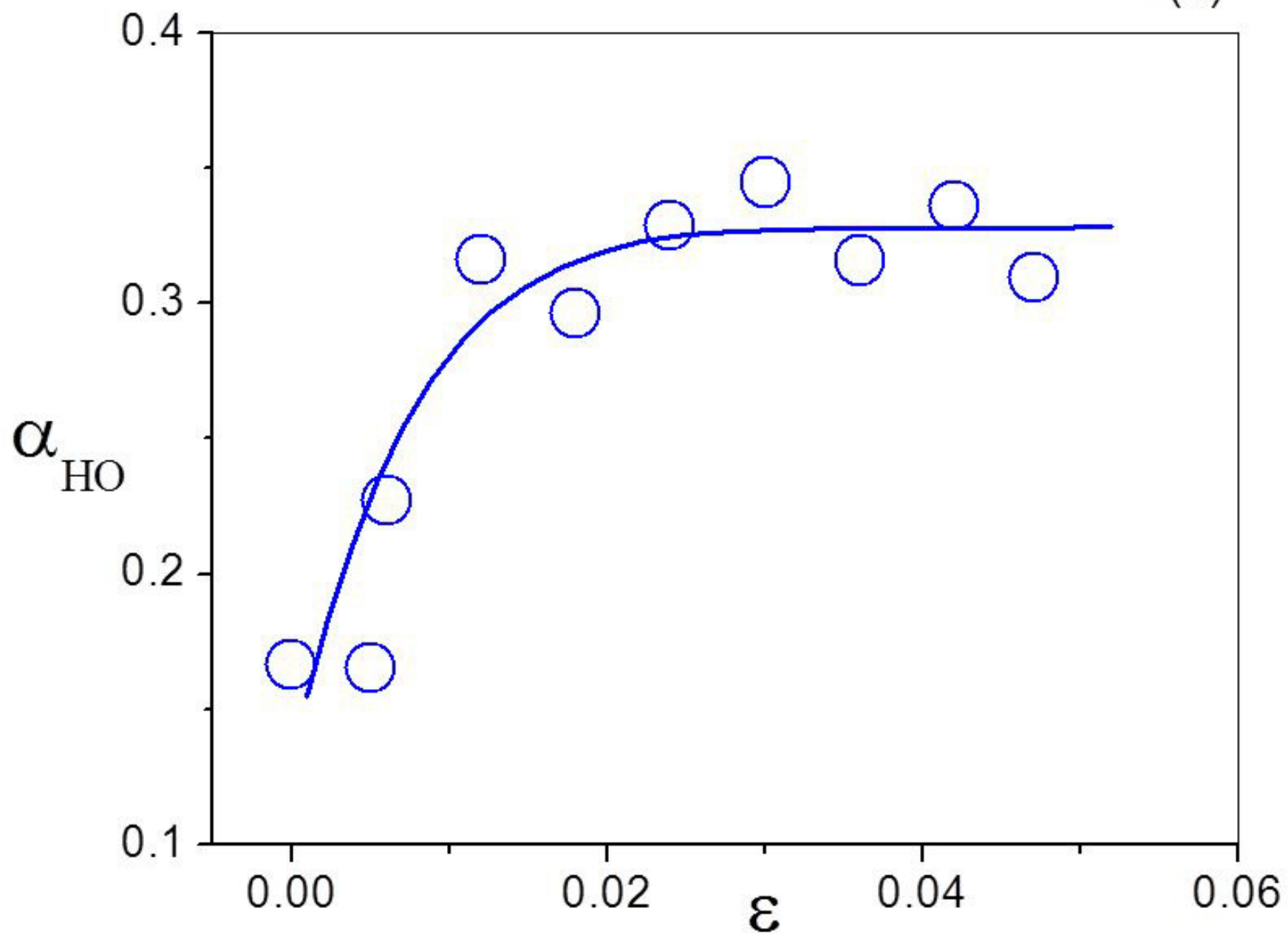


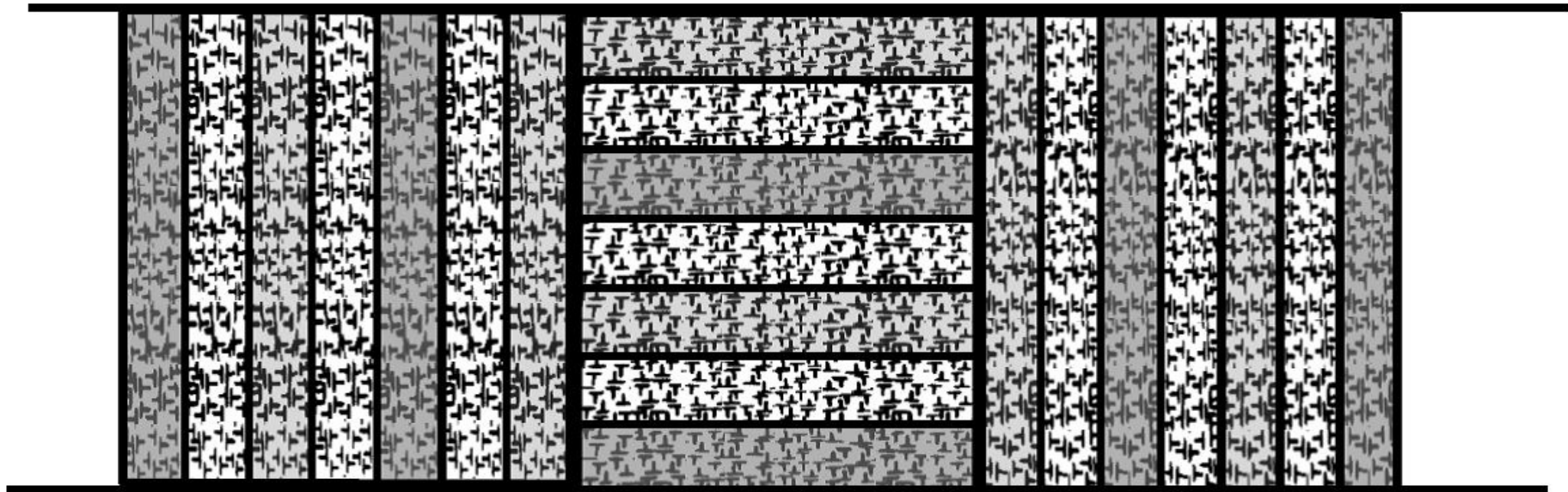
(a)



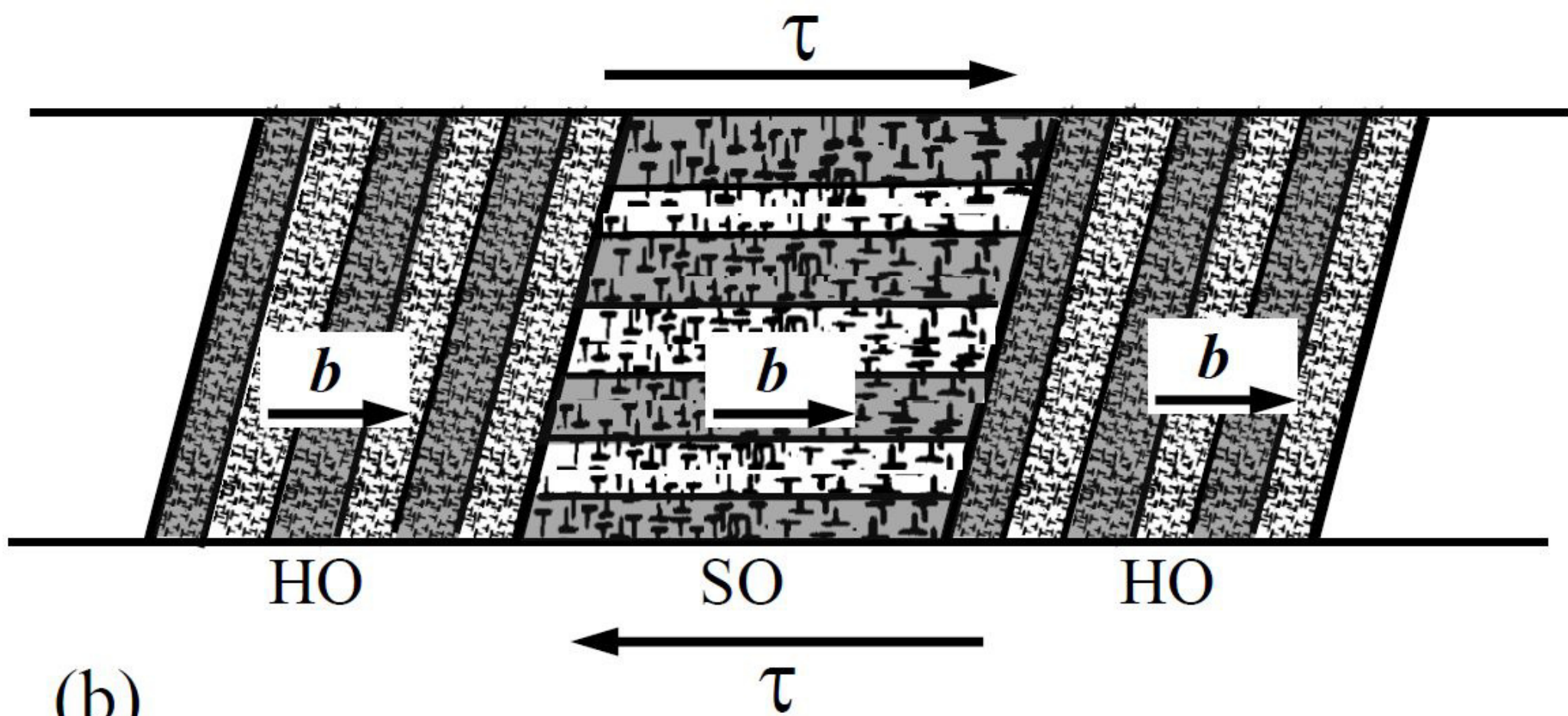


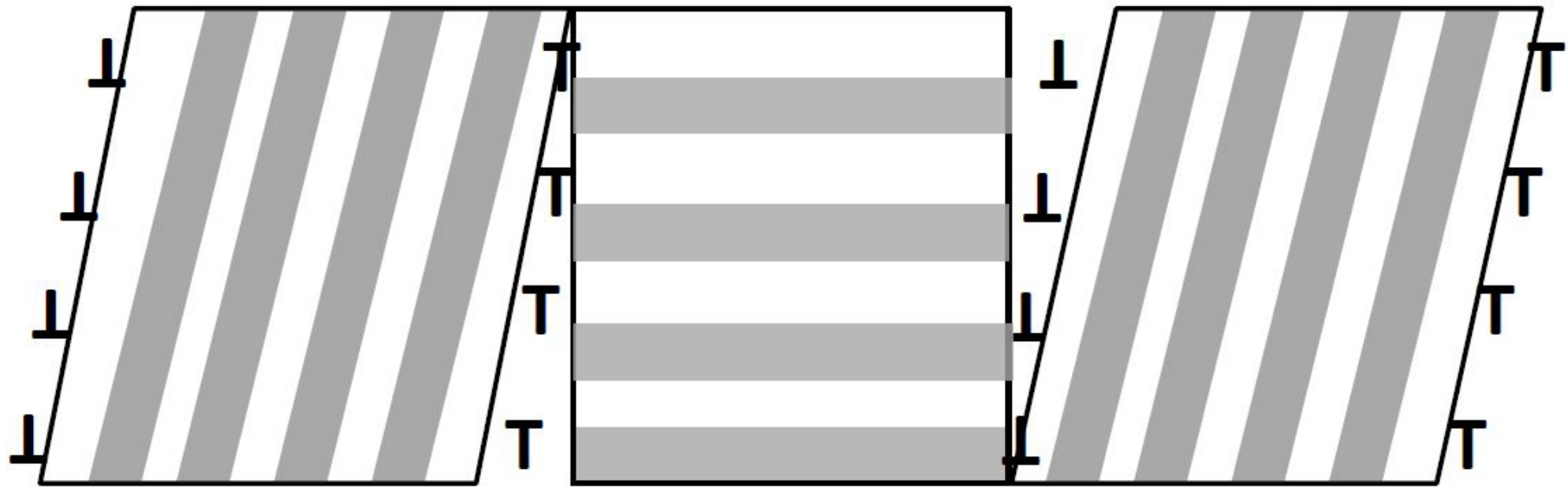
(c)





(a)



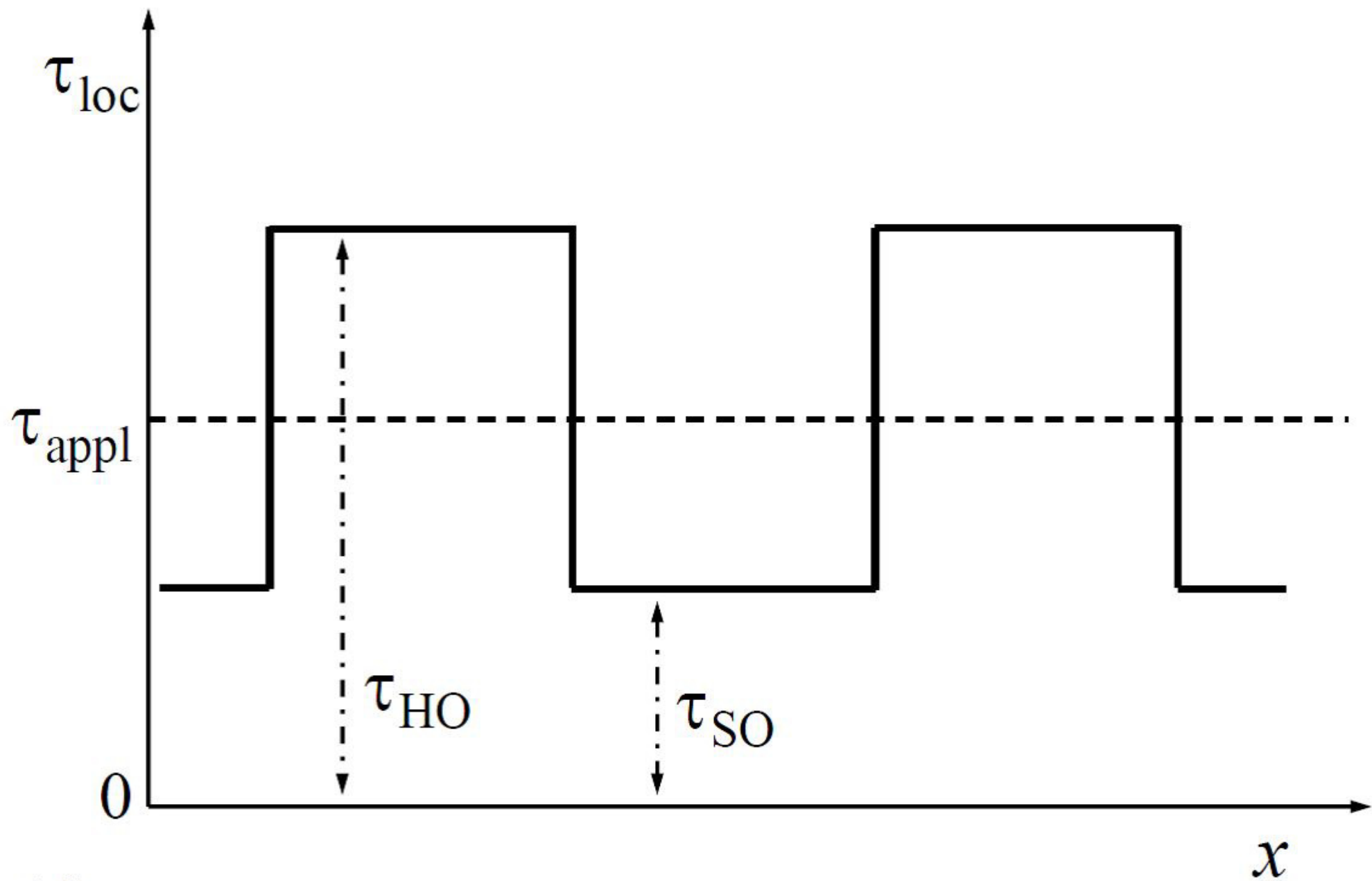


(c)

HO

SO

HO



(d)